Vertical coupling by solar semidiurnal tides in the thermosphere from ICON/MIGHTI measurements

Jeffrey M. Forbes[1], Jens Oberheide[2], Xiaoli Zhang[1], Chihoko Cullens[3], Christoph R. Englert[4], Brian J. Harding[5], John M. Harlander[6], Kenneth D. Marr[4], Jonathan J. Makela[7], and Thomas J. Immel[5]

[1]Ann and H.J. Smead Department of Aerospace Engineering Sciences, University of Colorado, Boulder, CO

[2]Department of Physics and Astronomy, Clemson University, Clemson, SC

[3]Laboratory for Atmospheric and Space Physics, University of Colorado. Boulder, CO

[4]Space Science Division, U.S. Naval Research Laboratory, Washington, DC

[5]Space Sciences Laboratory, University of California Berkeley, Berkeley, CA

[6]Saint Cloud State University, St Cloud, MN

[7]Department of Electrical and Computer Engineering, University of Illinois at Urbana-Champaign, Urbana, IL

Key Points:

- The latitude vs. day of year (DOY) variability of the semidiurnal tidal wind spectrum at 6°S-39°N and 250 km is depicted for the first time.
- Height vs. latitude and height vs. DOY depictions of non-migrating semidiurnal tidal propagation are presented for the first time.
- New insights into tidal vertical evolution due to dissipation and thermospheric sources of tides are provided.

Corresponding author: Jeffrey M. Forbes, `forbes@colorado.edu`

Abstract

Wind measurements from the Michelson Interferometer for Global High-resolution Thermospheric Imaging (MIGHTI) instrument on the Ionospheric CONnections (ICON) mission provide new insights into the semidiurnal tidal spectrum in the thermosphere, covering latitudes 9°S-39°N and altitudes 100-280 km altitude throughout 2020. Latitude versus day of year (DOY) variability of solar semidiurnal tides SE2, S0, SW1, SW2, SW3 and SW4 at 250 km are presented for the first time, and evaluated relative to similar results at 106 km. Using daytime-only data, height versus latitude and height versus DOY variability of SE2, S0, SW1. SW3 and SW4 amplitudes and phases are depicted for the first time, revealing the effects of a dissipative thermosphere on the vertical evolutions of these tidal structures. SW2 is absent from these depictions due to potential aliasing by zonal mean winds. The above results are considered in light of the Climatological Tidal Model of the Thermosphere (CTMT), which is based on fits to tidal winds and temperatures from the Thermosphere-Ionosphere-Mesosphere Energetics and Dynamics (TIMED) mission between 80 and 120 km during 2002-2008, and extrapolated to an altitude of 400 km based on modeled tidal structures propagating in a dissipative thermosphere, but without in-situ sources of excitation due to tide-tide or tide-ion drag nonlinear interactions. On the basis of comparisons with the CTMT and other characteristics revealed in the MIGHTI tidal structures, it is concluded that in-situ sources exist for S0, SW1, SW2 and SW3 in the thermosphere above about 200 km.

1 Introduction

In terms of atmospheric dynamics, the region between 100 and 200 km is the least explored in Earth's atmosphere, referred to as the "thermospheric gap" by Oberheide et al. (2011a). According to theory and modeling, it is within this region where gravity waves (GWs), vertically-propagating solar and lunar tides, planetary waves and ultra-fast Kelvin waves (UFKWs) dissipate and deposit momentum into the background atmosphere, introduce wind shears that produce layering of ionization (i.e., "sporadic-E"), and generate electric fields that map into the F-region and redistribute plasma through transport by $\mathbf{E} \times \mathbf{B}$ drifts. A subset of this vertically-propagating wave spectrum can also penetrate to F-region heights, and modify plasma distributions through field-aligned transport by neutral winds. The focus in this paper is on the height-latitude evolution of solar semidiurnal tides with periods of 12.0 hours derived from wind measurements made by the MIGHTI instrument on ICON during 2020.

Solar tidal variations in atmospheric variables such as winds, temperature and pressure are commonly expressed in the form

$$A_{n,s}cos(n\Omega t + s\lambda - \phi_{n,s}) \tag{1}$$

where $A_{n,s}$ is the amplitude; n = 1, 2, 3 refers to diurnal, semidiurnal and terdiurnal periods, respectively; $\Omega = 2\pi$ d^{-1}; s is the zonal wavenumber; λ is longitude; and $\phi_{n,s}$ is the phase (time of amplitude maximum at $\lambda = 0$, or longitude of maximum at t = 0). Setting the quantity in parentheses equal to a constant and differentiating yields the zonal phase speed of the tide, $C_{ph} = -n\Omega/s$. A solar-synchronous tide that follows the westward motion of the Sun to a ground-based observer ($-\Omega$, i.e., $s = n$), is traditionally referred to as a migrating tide; otherwise it is solar-asynchronous and is said to be non-migrating (Chapman and Lindzen, 1970). According to this convention, westward(W)-propagating ($C_{ph} < 0$) and eastward(E)-propagating ($C_{ph} > 0$) semidiurnal tides correspond to $s > 0$ and $s < 0$, respectively, and are simply denoted SWs and SEs without the sign of s included. The zonally-symmetric ($s = 0$) semidiurnal tide is denoted as S0. Similarly, diurnal and terdiurnal tides are referred to with 'D' or 'T' relating 'S' in this nomenclature. Note that a stationary planetary wave with zonal wavenumber s (SPWs) corresponds to $n = 0$.

Early work (Yanowitch, 1967; Lindzen, 1968; Richmond, 1975) recognized that exponential growth of GWs and tides is curtailed by viscous dissipation somewhere above ~100 km altitude depending on the vertical wavelength (λ_z). An important reference altitude is where the viscous term in the horizontal momentum and heat equations is of same order as the inertial term, or where

$$\chi = \frac{4\pi^2}{\lambda_z^2}\frac{\mu_0}{\rho\omega} \sim 1 \tag{2}$$

where λ_z is the vertical wavelength; μ_0 is the coefficient of molecular viscosity; ρ is the total mass density, an exponential function of height; and ω is the wave frequency, equal to $n\Omega$ for solar tides. According to equation (2), waves with longer λ_z encounter viscous dissipation at higher altitudes than waves with smaller λ_z. For λ_z of 30, 50, 70, 90 and 110 km, the altitudes where $\chi \sim 1$ are, roughly, 145, 162, 177, 190 and 200 km, for the NRLMSISE-00 empirical atmosphere (Picone et al., 2002) where the 10.7-cm solar radio flux F10.7 = 110 s.f.u. However, for tides another important influence is that of the planetary rotation rate. As shown analytically by Richmond (1975) and confirmed numerically in a one-dimensional "equivalent gravity wave" model by Forbes and Hagan (1979), the altitudes where tides with various λ_z curtail their growth and essentially reach their peak amplitudes can be 10's of kms lower than where $\chi \sim 1$. Moreover, according to analytic calculations without rotation the ratio of λ_z to the mean scale height (H) affects the shape of the profile above the peak (e.g., Lindzen, 1968, 1970), and produces reflection of order $exp(-2\pi^2 H/\lambda_z)$ (Yanowitch, 1967; Lindzen, 1968). For H = 7 km, this implies >25% reflection for $\lambda_z > 100$km, which applies to some of the tides to be considered here. However, these analytic approaches parameterized molecular dissipation, which involves second-order vertical derivatives of winds (molecular viscosity) in the momentum equations, and temperature (molecular thermal conductivity) in the thermal energy equation, with a single linear damping coefficient ("Newtonian cooling") inversely proportional to ρ in the thermal energy equation.

Hong and Lindzen (1976), Lindzen et al. (1977) and Forbes and Hagan (1982) sought to better understand and quantify the influences of thermospheric dissipation on vertically propagating tides, with emphasis on the solar semidiurnal migrating tide, SW2. They used a linearized tidal model (Forbes and Garrett, 1976) for a spherical, rotating, viscous, horizontally-stratified thermosphere with anisotropic ion drag to determine the upward extensions of classical tidal modes propagating into the thermosphere. In terms of tidal interactions with a viscous thermosphere, this approach replaces the earlier Newtonian cooling parameterization with an 8th-order system of differential equations, allows for thermospheric tidal structures that are inseparable in height and latitude; that is, horizontal structures vary with height, or equivalently, height structures vary with latitude. However, horizontal stratification implies that background winds are zero. Forbes and Hagan (1982) adopted more realistic parameterizations of ion drag, and coefficients of molecular conductivity and viscosity, that reduced the solar cycle dependences predicted by Lindzen et al. (1977). Following Lindzen et al. (1977), to this day we refer to the thermospheric temperature and velocity fields consistent with a conventionally-defined Hough mode from classical tidal theory as the "Hough Mode Extension" (HME) of that mode. Compared to prior work, HMEs better characterize the height at which each tidal mode maximizes in the thermosphere, and predicts the change in horizontal(vertical) shape with height(latitude) of that extended tidal mode due to thermospheric dissipation.

At the time of HME development, non-migrating tides, which define the longitude dependence of the atmosphere's tidal response, were not a subject of research. It was not until the satellite era that the longitude dependence of tides could be quantified (i.e., zonal wavenumber content; cf. Equation (1)). This enabled satellite-based determinations of tides to be least-squared fit with HMEs as the basis functions, leading to theoretical extrapolations of tidal behavior outside the height and latitude domain of the satellite measurements (Svoboda, et al., 2005; Oberheide et al., 2011a). In fact, Oberheide's (2011a) work, which fits HMEs to migrating and non-migrating tides determined from TIMED temperature and wind measurements below 120 km and equatorward of 72° latitude, forms the basis of the Climatological Tidal Model of the Thermosphere (CTMT), which characterizes the global behavior of vertically-propagating tides in the thermosphere (90-400 km; pole to pole). However, the height-latitude tidal structures contained within the CTMT have never really appeared to any significant degree in the literature, likely due to the absence of any measurements for comparison. The MIGHTI observations presented in the present paper provide the first opportunity for such a comparison, and in fact the CTMT can provide insights into the interpretation of the MIGHTI-derived tides. The CTMT and the HMEs which comprise it, are described in more detail in Section 2.

The possibility also exists that some semidiurnal tides can be generated in-situ within the thermosphere. For instance, we know from modeling that SE2 can be generated through nonlinear interaction between DE3 and DW1 in the lower thermosphere (Hagan et al., 2009). However, during solar minimum DE3 is capable of penetrating to much higher altitudes (Oberheide et al., 2009), and DW1 can take the form of in-situ winds or ion drag that are forced by the absorption of EUV radiation. Through the same reasoning explained in more detail later in this paper, a similar interaction between DE1 and DW1 can produce S0. SW1 and SW3 can also arise due to SW2 nonlinear interaction with SPW1, the latter in the form of zonal magnetic field and ion drag variations in the geographic coordinate system (Jones et al., 2013). In this paper we will remain cognizant of these potential additional in-situ sources (the effects of which are absent in the CTMT) as we interpret the evolution of amplitude and phase structures with height.

To summarize, the potential effects of dissipation on the vertical propagation of tides in the thermosphere have been realized for a long time, but only within the context of modeling efforts with varying assumptions and degrees of sophistication, as described above. In particular, the theoretical expectation (as embodied in a single HME) is that the effects of rotation combined with the $1/\rho$ dependence of viscosity on the vertical and horizontal structure of a tidal mode propagating into the thermosphere will be largely determined by its period and λ_z as suggested in equation (2). However, in accord with linear tidal theory, a tide as defined by its n and s (as in equation (1)) consists of a superposition of modes (or, HMEs in the thermosphere) each with its own horizontal and vertical structure. One can envision that the height-latitude structure of such a tide can be quite complex if a superposition of multiple HMEs is required to capture it. However, observations of thermospheric tidal structures have not yet been available to test the above concepts and assertions.

In this research we bring the first observation-based insights to the problem. Specifically, we elucidate the height-latitude structures of solar semidiurnal tides SE2, S0, SW1, SW2, SW3, and SW4 from 100 to 280 km between 9°S to 39°N latitude during 2020, and use HMEs and the CTMT to interpret them within the theoretical framework just described. These semidiurnal tides are the largest observed by MIGHTI during 2020, and identify with those comprising tidal climatologies based on TIMED measurements below 110 km (e.g., Truskowski et al., 2014; Oberheide et al., 2011a). For this select subset of the vertically-propagating wave spectrum, MIGHTI measurements provide the following first views of semidiurnal amplitudes and phases in the thermosphere: latitude versus DOY variability contemporaneously near 106 km and 250 km altitude; height versus latitude variability between 6°S-39°N and 100-280 km at select DOY; and height versus DOY variability at select latitudes. In the interest of brevity and efficiency, these depictions will be referred to as "latvsdoy", "htvslat", and "htvsdoy", respectively, throughout this paper.

The following section describes the MIGHTI wind measurements, the methodology through which semidiurnal tides are extracted from the data, and more details on HMEs and the CTMT. Results for each of the semidiurnal tides described above are presented and discussed in Section 3.

2 Data and methodology

2.1 ICON/MIGHTI wind data

The winds utilized in this study are Version 04 (V04) eastward (u) and northward (v) wind measurements from the MIGHTI (Michelson Interferometer for Global High-resolution Thermospheric Imaging) instrument (Englert et al., 2017) between -9° and +42° geographic latitude and 97 to 283 km altitude during daytime hours (~0600h-1800h). They are derived from two perpendicular tangent-point line-of-sight (LOS) vector measurements on the limb by observing the Doppler shift of the 557.7 nm "green-line" and 630.0 nm "red-line" emissions of atomic oxygen, which enable good quality wind retrievals between about 94-210 km and 160-300 km, respectively. The winds are measured to a precision of order 1.2-4.7 ms^{-1} (Harding et al., 2017), and have been validated against ground-based measurements (Harding et al., 2021; Makela et al., 2021). We have found that red-line and green-line winds can be combined together in the overlap region with no resulting discontinuities, which results from the use of a common zero-wind reference for both red-line and green-line winds (Harding et al., 2021; Makela et al., 2021). The 97 km and 283 km altitude limits are chosen to accommodate 6 km binning in altitude, such that the lower and upper altitudes in later plots fall on the center points of the 100±3 km and 280±3 km bins. Hereafter we simply refer to these altitude limits as 100 km and 280 km, which differ from the 94 km and 300 km limits of "good quality wind retrievals" in the interest of conservatively ensuring adequate coverage for the extraction of tides.

Data quality is handled as follows. The MIGHTI wind data that are not flagged as "bad" (wind_quality = 0) are either categorized as = 0.5 (Caution), or = 1 (Good). Many of the 0-flagged data are connected with South Atlantic Anomaly (SAA) contamination, and their removal leaves gaps between about 270-330 deg longitude in the Southern Hemisphere (SH). Wind_quality = 0.5 can also occur in the SAA, near the terminators, or at the altitude extrema of the MIGHTI measurements. We have experimented with the use of data quality flags, including calibration flags, and found that better spatial-temporal coverage and wave specifications can generally be achieved by including wind_quality = 0.5 data provided that an outlier criterion is applied, i.e., that within a given fitting window, wind amplitudes 3 times the median value are excluded. Our experience shows that the outlier criterion is in fact more stringent than the 0.5-quality flag in that it removes more data. Any reduced coverage as a result of data rejection is compensated for by choosing an appropriate time window within which fitting for tides is performed (see below).

2.2 Data analysis methodology

A major goal of this paper is to provide depictions of tidal evolutions with height that reveal the influences of molecular dissipation and the potential contributions of in-situ sources. The way in which this goal is achieved is influenced by how the MIGHTI instrument samples the atmosphere, and what limitations atmospheric emissions impose on the instrument and therefore its ability to measure winds. For example, while 24-hour LST coverage is obtainable for wind measurements below about 110 km and above about 200 km, the only continuous coverage in the intermediary height region occurs during daytime (about 0600-1800 LST) by combining green-line and red-line wind measurements. This eliminates consideration of diurnal tides, but in principle admits the possibility of extracting higher-frequency tides.

An example of how MIGHTI samples the atmosphere in latitude and local time (0600-1800 LST) as a function of DOY is provided in Figure 1 for 140 km. This coverage is typical of both u and v and for other altitudes in the height region of interest. Measurements are generally made at 14-15 longitudes per day at a given latitude, except in the SH where data gaps occur due to contamination associated with the South Atlantic Anomaly. Our methodology for determining adequacy of latitude, longitude and LST coverage for tidal fitting within a given “window” of time rests on two points. First, for altitudes near the upper and lower extrema of 100 km and 280 km considered in this study, full 24-hour LST coverage is available over a wide range of latitudes. Considering the occurrence of occasional gaps associated with the SAA, data quality considerations, and instrument calibrations (cf. Figure 1), the satellite orbit and MIGHTI observing geometry ensure that stable extractions of solar tides can be consistently obtained within a 41-day (hereafter 41d) moving window throughout the year. This is basically determined by trial and error as in the study by Cullens et al. (2020). Second, the basic criterion for determining adequacy of *daytime* coverage was to perform two semidiurnal fits to the data near these two altitude extrema, one using data spanning 24h of LST, and the other using daytime-only data. If both fits captured the same salient amplitude and phase latitude structures given the range of uncertainties, then the daytime coverage was considered acceptable for tidal fitting at all the intermediate altitudes. However, it was also determined that this agreement sometimes required extending the fitting window to 61d, and/or contracting the SH latitude limit from 9°S to 6°S or to the equator. In addition, it was often the case that contour plots of tidal amplitudes and phases exhibited "edge effects" at the SH boundary of 9°S, likely a result of SAA effects, which also led to contracting the SH boundary to 6°S. Therefore, in the following, results are presented using either 41d or 61d fitting windows and variable SH latitude limits depending on the veracity of the daytime-only tidal fits and SAA influences. Implementation of this methodology is now described using SE2 as an example.

As the first step in the procedure that was followed, tidal fits within 41d and 61d moving windows were performed on winds averaged between 103-109 km and 230-270 km, also referred to as "106 km" and "250 km" hereafter. The height ranges were chosen instead of single altitudes to remove the effects of small-scale variations, to improve statistics and to enable smoother visual depictions. For similar reasons and to reduce SAA influences, prior to tidal fitting data were binned in 6° latitude bins every 3° latitude extending from 6°S to 39°N; 40° longitude bins every 20° latitude; and 2h UT bins centered on each of 24h. This same binning was performed in 6 km altitude increments slid every 3 km from a center point at 100 km up to a 280 km center point. Tidal fits to the binned data enabled construction of height versus latitude hereafter ("htvslat") contour depictions of amplitude and phase (hereafter "amp/phz") to be constructed. Standard deviations for each bin centered on -9°, 0°, +9°, +18°, +27°, and +36° latitude were saved, and used to estimate uncertainties in the amp/phzs obtained from the fits, and to enable vertical profiles of amp/phz to be constructed for comparison.

Uncertainties in the amp/phzs noted above are calculated as follows. In our semidiurnal tidal fitting, each wave is specified by a pair of cosine and sine terms as in (1). The 1-σ uncertainty of each term is estimated by $\sqrt{var}$ where var is the variance of that term, standard output from the least-squares fitting algorithm based on the residuals from the fit. The 1-σ uncertainty of amplitude is calculated by $\sqrt{a^2 \cdot a_v + b^2 \cdot b_v}/A$ while the 1-σ uncertainty of phase ϕ is calculated by $\sqrt{b^2 \cdot a_v + a^2 \cdot b_v}/A^2$ where a and b are the fitting coefficients of cosine and sine terms, respectively; a_v and b_v are the variance of cosine and sine terms, respectively; $A = \sqrt{a^2 + b^2}$ and $\phi = \tan^{-1}$(b/a).

The latvsdoy depictions of SE2 amplitudes resulting from the binning and fitting described above are shown in the top panels of Figure 2 for 6°S to 39°N and 61d means (hereafter 61dm). The 61dm choice conforms with the temporal resolution of the CTMT, which serves as a climatological reference of the vertically-propagating tidal spectrum without contributions from in-situ sources (see details below), and which moreover differs in minor details from the 41dm results. Comparisons between 106 km and 250 km results in Figure 2 clearly indicate that vertical evolutions in the SE2 amplitude structure exist that are latitude dependent, and it is these vertical evolutions that represent the core of the present investigation. It is furthermore evident that the CTMT latvsdoy structures in the bottom panels of Figure 2 do not bear much resemblance to the MIGHTI structures, although the amplitudes are similar in magnitude overall.

As a next step in the data processing sequence, periods of time were selected that overlap with the major maxima in Figure 2 *and* passed the daytime-only fitting "veracity test" discussed above. The midpoints of these periods of time are indicated by vertical dashed lines in Figure 2. Figure 3 provides a few examples of how these were selected, focused again on SE2. The left column provides comparisons between amp/phz latitudinal structures obtained with 61d fitting to v winds with 24h LST coverage (red lines/symbols) with 61d fitting to v winds with daytime-only (13h LST) coverage at "106 km" (top 2 rows) and "250 km" (bottom 2 rows) for the period of time centered on DOY 120. Note also that this agreement extends from 9°S to 39°N in this case. Given the indicated uncertainties, the uniformity of LST coverage with altitude, and the fact that these curves cannot be expected to agree exactly since they are based on different samplings of the same waveform, the two curves were objectively judged to agree sufficiently well to draw scientific conclusions based on 13h fits at all intermediate heights. After examination of all available such comparisons between 13h and 24h fit results at two altitudes, it was concluded that there is not a quantitative measure of agreement as informative as visual objective evaluation.

The middle column of Figure 3 shows a similar result and conclusion for v based on comparisons between 41d fitting to 24h LST coverage (black lines, symbols) and 41d fitting to daytime-only data (blue lines/symbols) for DOY 240. In this case, the southern latitude limit is the equator. The third column shows a similar comparison for u, except for fitting to 61d of data within 30±5° latitude bins centered on every 30 DOY, and which correspond to the horizontal dashed lines in Figure 2. This enables a depiction of the htvsdoy amp/phz structures of SE2 corresponding to the single latitude region of 30±5°N. The htvslat and htvsdoy amp/phz structures of SE2 that correspond to the dashed lines in Figure 2 are discussed and interpreted in the next section, along with other tidal components obtained by the same methodology.

The degrees of agreement depicted in Figure 3 are typical of those of other non-migrating tides considered in this paper. No satisfactory results could be obtained with the above methodology for the migrating semidiurnal tide, SW2. It is our interpretation that aliasing by zonal- and diurnal-mean winds, which vary considerably within the 41d and 61d fitting windows, into the daytime-only tidal determinations is the cause of this discrepancy. Therefore, the analysis of SW2 will take a more limited form in this paper, focusing just on the 106 km and 250 km results.

2.3 Hough Mode Extensions (HMEs) and Climatological Tidal Model of the Thermosphere (CTMT)

The CTMT is an empirical model of solar diurnal and semidiurnal tides propagating upward from the lower atmosphere. It extends from 80 to 400 km and from pole to pole, and specifies temperature, density, and zonal, meridional and vertical wind perturbations for a number tidal components identified in 2002-2008 averaged temperature and wind measurements in the mesosphere-lower thermosphere (MLT) region made by the Sounding the Atmosphere using Broadband Emission Radiometry (SABER) and TIMED Doppler Interferometer (TIDI) instruments, respectively, on the TIMED satellite. The CTMT is based on least-squares fits of theoretical tidal functions ("Hough Mode Extensions", or "HMEs") to 60d-mean TIDI tidal winds between 80-105 km and $\pm 75°$ latitude and 60d-mean SABER tidal temperatures between 80 and 105-120 km altitude and $\pm 50°$ latitude, which are then superimposed for a given $n\Omega$ and s to capture the 60d-mean height-latitude structure of that tide centered on the 15th of each month. The CTMT and its HMEs are used here to provide a climatological model context for the results presented herein, and to aid in the interpretation of the MIGHTI-based tidal structures between 106 and 250 km. The fact that the CTMT tidal structures extend from pole to pole and include both u and v adds to its utility in terms of interpreting the MIGHTI tidal structures over the 9°S-39°N latitude region, as demonstrated below.

HMEs (Lindzen et al., 1977; Forbes and Hagan, 1982) represent the 2-dimensional (htvslat) extensions into the dissipative thermosphere of the Hough functions of classical tidal theory (Chapman and Lindzen, 1970), which are derived based on the separability of the linearized tidal equations in a horizontally-stratified atmosphere without dissipation. HMEs are solutions to the linearized tidal equations where all dissipative processes (i.e., eddy and molecular diffusion, ion drag) and background atmospheric conditions (density, temperature and pressure) are latitude-independent. Tropospheric heating with the latitude shape (Hough function), $n\Omega$, and s of a given tidal mode are used to force each HME. The velocity, temperature and density (u, v, w, T, ρ) perturbation fields consequently possess internally self-consistent relative amp/phz relationships for any given HME. So, if a HME is least-squared fit to a distribution of u, v and T tidal amp/phzs (in complex form) for a given $n\Omega$ and s, a single complex normalizing factor emerges that sets the amp/phzs for all variables at all latitudes and heights for that HME.

In the CTMT the semidiurnal tides of interest in the present paper are all based on reconstructions based on fits to 4 HMEs. They are generally in the sequence 1st symmetric (HME1), 1st antisymmetric (HME2), 2nd symmetric (HME3), 2nd antisymmetric (HME4), and so on, each subsequent HME decreasing in vertical wavelength (λ_z) and increasing numbers of maxima and minima in the horizontal structures. For zonally-symmetric $s = 0$ tides, the first in the sequence (HME1) is antisymmetric and alternates thereafter. For later reference, Table 1 provides λ_z, altitudes of peak amplitude, and locations of the u and v latitudinal maxima for the 4 HMEs corresponding to SE2, S0, SW1, SW2, SW3, SW4. The term "vertical wavelength" as used here refers to a local measure of phase progression, and represents an extrapolation to the full 12-hour cycle of the semidiurnal tide based on the average phase gradient within a given height range. The λ_z in Table 1 are provided to assist in identifying the correspondence of particular HMEs with observed tidal structures, and the potential degree of vertical penetration of those tidal components to higher levels in the thermosphere. For many of the HMEs, the λ_z listed in Table 1 are obtained from the phase gradients between 90 and 110 km. However, for the longest-wavelength HMEs, we found that definition to not be representative, due to apparent effects of changes in temperature structure and/or wave reflection on the phase progression, or because the phase changes were too small within 90-110 km to get a reliable measure of λ_z. In these cases, indicated with an asterisk hereafter and in Table 1, the phase change over height range 102 to 151 km was used to get λ_z.

SE2 is used again as a first example that can serve as a reference for the remaining tides considered in this paper, and accordingly the first four HMEs for u and v for SE2 are depicted in Figure 4. Similar plots for the S0, SW1, SW2, SW3 and SW4 HMEs are provided in the Supporting Information, and in all cases the absolute values of amps/phzs are arbitrary, but their relative amplitudes and phases are as depicted. Note that the number of maxima in latitude for u (and temperature, not shown) increases from 1 to 4 for HME1 to HME4; or equivalently the number of nodes in phase between the poles increase from 0 to 3. Also, when u and T are symmetric, v is antisymmetric, and vice-versa. From Table 1, λ_zs for SE2 u decrease (195 km, 87 km, 54 km, 39 km) as the HME order increases (HME1, HME2, HME3, HME4). Decreases in the altitudes of maxima (199 km, 133 km, 114 km, 114 km) occur in accord with decreases in λ_z and the altitude where $\chi \sim 1$ from expression (1), and subject to additional reductions in peak altitude due to the effects of planetary rotation. Similar behaviors apply for v and T, and for all HMEs. Another effect introduced by viscous dissipation is the increased latitudinal broadening of horizontal structures that occurs as altitude increases; that is the latitudinal maxima migrate poleward with increasing altitude (see, e.g., Lindzen et al., 1977; Forbes and Hagan, 1982). This is especially evident in u for HME1, HME2, HME3 and in v for HME1 in Figure 4, and is also generally characteristic of HMEs for S0, SW1, SW2, SW3 and SW4.

It is interesting to note that the phase behaviors below and above $\sim$100 km are different for HME3 and HME4 on the one hand, and HME1 and HME2 on the other. That is, HME3 and HME4 have short λ_zs below the thermosphere, which lengthen as molecular dissipation becomes important at higher altitudes. Recall that increasing viscosity with height becomes more and more efficient in removing vertical shears. However, HME1 and HME2 have extremely long (comparatively, “near-infinite”) vertical wavelengths below $\sim$100 km, then suddenly switch to relatively short vertical wavelength just above 100 km, followed by lengthening above $\sim$150 km. Similar behaviors are shared by the HME1s for DE1, SE3, SE1, SW1 and SW2, and are thought to be connected with the temperature structure and/or reflection effects mentioned in the Introduction that apply to these long-wavelength tidal components. Given the results of Richmond (1975) and Forbes and Hagan (1979), and the fact that the effects of rotation enter through the Coriolis parameter, the effects of rotation on wave reflection are expected to be significant and latitude-dependent.

There are a few potential caveats to keep in mind concerning the use of the CTMT to interpret the MIGHTI tidal structures to be presented in Section 3. First, it is noted that the CTMT is based on HMEs calculated for background atmospheric conditions corresponding to a 10.7-cm solar flux (F10.7) of 110 s.f.u., whereas the mean F10.7 for 2020 is approximately 75 s.f.u.. Based on comparisons between DE3 HMEs for F10.7 values of 60 and 110 in Oberheide et al. (2009), and unpublished HMEs for SE2 and SW2 created at that time, this difference in prevailing solar conditions does not significantly affect tidal specifications below roughly 150 km, but can potentially increase amplitudes at 250 km relative to the CTMT, especially for low-order HMEs. In addition, in the actual implementation of HME fitting within the CTMT (Oberheide et al., 2011a) and related preliminary work (Oberheide et al., 2008), an empirical adjustment factor of 0.93 to the HME altitudes was applied in order to optimize the overall fit to TIMED measurements. This had the effect of lowering the peak altitudes of the employed HMEs compared to those actually calculated. The latter are what appear in Table 1, since this adjustment did not appear necessary in the present analysis. In the following section where results are presented and interpreted, the CTMT will therefore be employed more qualitatively than quantitatively in the interpretation of MIGHTI-based tidal structures. More details of the CTMT and HMEs are provided in the paragraphs below.

For completeness we must add one additional caveat to the use of CTMT and HMEs in the interpretation of latitude and vertical structures of observed tides, and that is that those structures can in principal be affected by zonal-mean zonal winds, ($\bar{U}$). From GCM modeling studies (e.g., Ekanayake et al., 1997; Gasperini et al., 2017) eastward-propagating(westward-propagating) diurnal tides tend to propagate into regions of westward(eastward) $\bar{U}$ and thus shift their latitudinal maxima. These shifts are accompanied by lengthening(shortening) of λ_zs, decreased(increased) dissipation vis-a-vis (1), and consequently modified vertical amplitude and phase structures. (see also Forbes, 2000, for discussion of similar effects for the 3-day UFKW). No such studies have been directed towards semidiurnal tides, but some rough assessments of potential $\bar{U}$ impacts can be made if we consider that the magnitude of such effects becomes significant if $\bar{U}$ is comparable to the zonal phase speed of the tide (C_{ph} = -$\frac{n}{s}463\cos\theta$ ms^{-1}). If we define $I = |\bar{U}|/|C_{ph}|$, and assume nominal values of $\bar{U} = 25$ ms^{-1} (based on the Horizontal Wind Model 2014 (HWM14), Drob et al., 2015) and θ=18°, then I = 0.12 for SW4, 0.09 for SW3, 0.06 for SE2 and SW2 and 0.03 for SW1. As a point of reference, the GCM simulations of DE3 by Gasperini et al. (2017), which correspond to I $\approx$ 0.34 for $\bar{U} \sim 50$ ms^{-1}, yield ∼15° horizontal displacements of the horizontal structure of DE3 within the ±30° latitude region, which are significant. By comparison the above rough estimates suggest that mean wind effects for the semidiurnal tides of interest are likely of secondary importance but perhaps not negligible depending on the magnitude of $\bar{U}$ in comparison to 25 ms^{-1}. S0 is not expected to be significantly affected by $\bar{U}$ since it is not Doppler-shifted. For reference, the latvs-doy depictions of $\bar{U}$ for HWM14 at 106 km and 250 km, the magnitudes of which are typical of those throughout the 100-280 km domain, are provided in Supporting Information Figure S1-HWM14. The HWM14 model values are used here instead of MIGHTI-derived values, since improvements are still being made on the zero-wind baseline for MIGHTI winds, to appear in Version 05.

It should also be noted that the use of HMEs to fit or interpret observed htvslat tidal structures (as in the following section) assumes that the salient features of such structures can be captured by the linear superposition of a few HMEs, provided that tides produced by in-situ sources are negligible. A number of studies have indeed demonstrated that a linear superposition of HMEs can capture much of the coupled htvslat tidal structures in both observational data and general circulation models (e.g., Svoboda et al., 2005; Cullens et al., 2020; Oberheide et al., 2011a,b), but so far such fitting has only been applied below about 110 km. For diurnal tides, only 2 HMEs are generally required since higher-order HMEs have short vertical wavelengths and do not penetrate effectively above 100 km (Oberheide et al., 2011a). Oberheide et al. (2009, 2011b) were very successful in predicting and interpreting DE3 and SE2 tides near 400 km altitude in terms of HME extrapolations based on tidal fits below 110 km. For semidiurnal tides, 4 HMEs are generally required, which makes the interpretation of observed semidiurnal structures based on HMEs more complicated. In particular interference between co-existing HMEs tends to dominate the height versus latitude structures, making the inseparability effects of dissipation difficult to identify. Consistent with experience gained with the CTMT, interpretation of MIGHTI semidiurnal tidal structures in the next section are performed within the context of a linear superposition of 4 HMEs. This will be the first attempt at interpreting semidiurnal tidal structures in the lower and middle thermosphere region of 106-250 km, and should provide valuable insights into the whole concept of HMEs and the assumptions underlying their application.

3 Results

In the following subsections 3.1 to 3.6, the vertical and latitudinal structures of SE2, S0, SW4, SW1, SW2, and SW3, respectively are depicted and analyzed in various forms.

In order to draw conclusions regarding the nature and origins of these structures, the analysis requires delving into some specific details regarding HME and CTMT amp/phz structures. The reader interested in following these details and arguments is referred to HME plots for S0, SW1, SW2, SW3 and SW4 similar to those of Figure 4 for SE2, and to CTMT Figures complementary to those of Figures 2 to 19, in the Supporting Information, as well as to Table 1.

3.1 SE2

SE2 is thought to be primarily forced by the semidiurnal cycles of latent heating and solar radiation absorption in the troposphere, modulated by the predominant longitudinal wave-4 variation in land-sea difference (e.g., see Truskowski et al., 2014, and references therein; see also Zhang et al., 2010a,b, and Hagan and Forbes, 2003). Using the notation [n, s] to represent the cosine expression (1) for a tide or stationary feature (n = 0) such as a planetary wave, and expressing n in units day^{-1}(d^{-1}), then SE2 is expressed simply as [2, -2]. The modulation of migrating solar semidiurnal heating (SW2) by a wave-4 land-sea difference (SPW4) can then be represented as: SPW4 $\times$ SW2 = [0, +4] $\times$ [2, +2] $\rightarrow$ [2, +6] + [2, -2] = SW6 + SE2. Note that the resulting waves are characterized by the sums and differences, respectively, of the frequencies and zonal wavenumbers of the primary interacting waves, and the same relationships between primary and secondary waves apply to interactions between tides and between tides and traveling planetary waves (Teitelbaum and Vial, 1991). Although prominent in the modeling work of Hagan and Forbes (2003), SW6 is not among the most important semidiurnal tides derived from the MIGHTI measurements, and is not considered further here. In a similar fashion, SE2 can arise through interaction between DE3 and DW1 in the lower thermosphere: DE3 $\times$ DW1 = [1, -3] $\times$ [1, +1] $\rightarrow$ [2, -2] + [0, 4] = SE2 + SPW4, as demonstrated through general circulation modeling by Hagan et al. (2009) and Pedatella et al. (2012). Forbes et al. (2021) demonstrated the presence of SPW4 and SE2 in ICON/MIGHTI winds at 106 km and 295 km, the potential for SE2 to propagate to F-region altitudes, and noted connections with contemporaneous topside F-region electron density variability observed by ICON. He et al. (2011) emphasized the importance of SE2 trans-equatorial winds to latitudinal asymmetries of ionospheric observations. Thus, SE2 is recognized as important for atmosphere-ionosphere coupling, both in terms of the electric fields and plasma drifts that it can generate, and in terms of its capability to redistribute of ionospheric plasma in-situ in the F-region through its meridional winds. Thus, there is a need to ascertain how and to what extent vertically-propagating SE2 can penetrate to higher altitudes in the thermosphere.

Figure 5 illustrates htvslat structures for 41dm v at DOY 240, and 61dm v at DOY 120, for SE2. For DOY 240, amp/phz profiles corresponding to 0° latitude are shown to the left, and for DOY 120 amp/phz profiles at +9° latitude are shown to the right of the htvslat contour plots. The amp/phz profiles are shown at latitudes near maxima in the htvslat plots, and consist of two sets of profiles. The black symbols/lines indicate the actual values to emerge from the least-squares fitting, and through the standard deviations indicated by the horizontal lines, provide a sense of the uncertainties in those values introduced by geophysical variability as embodied in the standard deviations of binned averages that were the subject of least-squares fitting. Since htvslat plots based on these values yielded sometimes ragged amplitude contours and phase jumps that served to distract from the more salient features, the real and imaginary parts of the raw-data amp/phz's were smoothed in the vertical, and then reconstructed to yield the smoother blue lines and symbols which formed the basis for the htvslat structures as shown.

On DOY 240 the amplitudes are concentrated near the equator, with the largest amplitudes near 115 km, 160 km and above 220 km. Between 115 and 280 km, amplitudes generally decrease away from the equator, reach minima around 24°-30° latitude, and then show signs of increasing towards higher latitudes. The times of maxima show downward progression, consistent with upward propagation. Vertical wavelengths increase with height, more(less) so equatorward(poleward) of about +24° latitude. The change in λ_z with latitude, combined with the noted amplitude structures, suggests the superposition of more than one HME.

Specifically, the large 12 ms^{-1} equatorial peak for v near 115 km (DOY 240) in the black-line profile (smoothed out in the htvslat depiction) and its accompanying $\sim$ 30 km λ_z suggest the presence of an antisymmetric mode, and SE2 HME4 with vertical wavelength of 39 km (Table 1) with an additional maximum near 36°N (Table 1) seems to be a candidate, although the higher-order HME6 (not included in Table 1) could be a possible contributor at the lowest altitudes, given the observed 30 km vertical wavelength. At the equator, HME4 decreases monotonically by 40%(36%) from 114 km to 220 km(280 km), and therefore suggests that most of the 6 ms^{-1} v amplitude over the equator at 220 km can be accounted for by HME4, but less than half the 8-10 ms^{-1} amplitudes at 280 km. This suggests that HME2 with amplitude of order 5 ms^{-1} might exist at 280 km, and given its broad vertical structure can potentially destructively interfere at a level of 5 ms^{-1} with HME4 near 135 km to produce the minimum in amplitude there. The generally broader latitude structure of SE2 v amplitude at the higher versus lower altitudes is consistent with the decrease in relative importance of HME4 versus HME2 with altitude.

As noted at the beginning of this subsection, it was stated that nonlinear interaction between DE3 and DW1 is capable of producing SE2. DW1 is ubiquitous in the thermosphere, and unpublished latvsdoy depictions of DE3 u at 250 km (similar to those in Figure 2) indicate equatorial-region amplitudes of order 6-7 ms^{-1} between DOY 150-270. Therefore, concerning the potential importance of HME4 and HME2 to account for the observed amplitudes between 220 km and 280 km, the possibility that an in-situ source may contribute at the altitudes, latitudes and DOY just quoted cannot be discounted. We return to this point in connection with Figure 7.

The height-latitude structure of CTMT for DOY 240 (Figure S5-CTMT) is also consistent with the dominant presence of HME2 above about 190 km and with higher-order HMEs at lower altitudes, with maximum amplitudes reaching $\sim$7 ms^{-1} at all altitudes, and decreasing monotonically away from the equator above about 160 km altitude. A distinctive feature of the CTMT climatological distribution of SE2 v below 130 km is a maximum between 6°N-18°N at about 115 km. However, HME1, HME2, HME3 and HME4 do not include a HME with v amplitudes maximizing at these latitudes. Referring to height-latitude structures between $\pm$60° latitude of SE2 at DOY 240 (not provided), it is clear that this structure arises as a result of constructive interference between HME4 and the second symmetric HME, HME3. Note from Table 1 that both of these HMEs possess maxima near 114 km, with HME3 maximizing at $\pm$24° latitude and HME4 maximizing at the equator and $\pm$36°. It follows that depending on the relative magnitudes and phases of HME3 and HME4 that the maxima in latitude would lie somewhere between the equator and $\pm$24°, and that the maxima in altitude would lie somewhere in the vicinity of 114 km. In fact, looking retrospectively at the MIGHTI v amplitudes for DOY 240, there exists a region of $\sim$4 ms^{-1} amplitudes between 6° and 12° latitude and 120-145 km altitude that could be attributable to some contribution by HME3 through the same reasoning.

The above examination of CTMT versus MIGHTI SE2 v structures for DOY 240 can now inform us about the nature of the SE2 v amp/phz structures shown in the right sides of Figure 5 and Figure S5-CTMT for DOY 120. Starting with the CTMT climatology, the dominant feature is a maximum between 110-115 km altitude and 12°-20°N latitude with vertical wavelength of order 50 km. The decrease in amplitude from the peak to 280 km is about 50%. The vertical wavelength remains approximately constant at latitudes $\geq$15°, and increases modestly equatorward of 15°. Examination of the htvs-lat structures extending out to ±60° (not provided) confirms the interpretation that the CTMT climatological structures are determined by the interference between HME3 and HME4 with some contribution by HME2. The MIGHTI SE2 v structure for DOY 120 in Figure 5 is in many respects similar to that of the CTMT; that is the dominant feature is a maximum in the lower thermosphere, decreasing to about 70% of its peak value by 280 km. The main difference is that the lower thermosphere peak occurs at about +6° latitude and 125 km altitude. We interpret this structure as reflecting dominance of HME4 with sufficient contribution from HME3 to move the maximum in the interference pattern between the two from the equator to 6°N, and to increase the altitude of maximum and the vertical wavelength. It is also possible that the effects of $\bar{U}$ could be a contributing factor in determining details of these structures.

The left panels of Figure 6 provide one additional insight into the htvslat structure of SE2, in this case for the 41dm u wind component centered on DOY 80. The main feature is a 9 ms^{-1} peak near 30°N latitude and 115 km altitude. HME3 with major(minor) peaks at ±36°(0°) latitude and 114 km altitude contains the same salient features. A similar structure exists in the CTMT (see Figure S6-CTMT) with 7 ms^{-1} peak at slightly lower altitude. Examination of the CTMT SE2 u and v htvslat structures between ±60° latitude provide evidence that HME3, HME4 and HME2 (in this order) are contributing to the CTMT climatological structure. The phase structures compare well between Figure 6 and the CTMT climatology. And, while the CTMT climatological amplitudes decrease monotonically with height whereas the MIGHTI u amplitudes increase slightly between 190 and 280 km, this difference occurs within the depicted amplitude uncertainties in Figure 6 and is therefore inconclusive.

An alternative view of SE2 is provided in Figures 7 and S7-CTMT, which depict the htvsdoy variability of 61dm SE2 amp/phz for v averaged over 0±5° latitude, and for u and v averaged over 30±5°. Also shown in Figure 7 are vertical amp/phz profiles with uncertainty estimates at the closest 9°-spaced sampled 3° grid points for which these data were saved, and for select DOY: v, 0°, DOY = 0; v, 0°, DOY = 300; u, 27°, DOY = 300; v, 27°, DOY = 300. All of the displayed vertical profiles indicate phase progression with height consistent with upward propagation. Although increases in amplitude sometimes occur above 200 km, it can be argued, at least for v, that these increases are plausibly accounted for by the vertical structure of v HME1 in Figure 4. And with the exception of the double maxima in v at 30° latitude around DOY 300 in Figure 7 (upper right panel), the htvsdoy amplitude and phases structures displayed in Figure S7-CTMT are very similar to those in Figure 7. This supports the other evidence in this subsection, that the MIGHTI winds primarily reflect vertically-propagating SE2 components from below, with occasional but relatively minor influences from the potential in-situ excitation sources mentioned earlier.

A likely example of an in-situ source contribution to SE2 exists around DOY 180 in the upper left panel of Figure 7 (v, 0° latitude) and to a lesser extent in the upper right panel of Figure 7 (v, 30° latitude). Focusing on 0° latitude, amplitudes of order 4-6 ms^{-1} exist between 220-280 km altitude without any apparent connection to a wave propagating upwards from below. This is likely further evidence of the in-situ source contribution from SE2 at DOY 240 more subtly suggested in connection with Figure 5. Note that the dotted line at DOY 240 in Figure 7 refers to the 41dm amp/phz vertical profiles on the left-hand side of Figure 5, which depicts more lower thermosphere wave activity than might be inferred from the 61dm results at DOY 240 in Figure 7.

3.2 S0

S0 has not received much attention in the terrestrial literature, although it is one of the more prominent semidiurnal tides in the Martian atmosphere (Forbes et al., 2020). By analogy with SE2, its origins lie in part in tropospheric heating (e.g., Hagan and Forbes, 2003), most likely the modulation of migrating solar semidiurnal heating (SW2) by the wave-2 land-sea difference (SPW2): SPW2 × SW2 = [0, +2] × [2, +2] → [2, +4] + [2, 0] = SW4 + S0. Note that SW4 is discussed in the next subsection. An equally viable source for S0 exists wherein SPW2 in the above interaction refers to a stratospheric SPW2, and SW2 refers to excitation of SW2 through heating by ultraviolet solar radiation absorption by stratospheric ozone, which is actually the main source of SW2 below 100 km altitude in Earth's atmosphere. By analogy with Mars, S0 can also arise from the following nonlinear interactions: DE1 $\times$ DW1 = [1, -1] $\times$ [1, +1] $\rightarrow$ [2, 0] + [0, 2] = S0 + SPW2 and DE2 $\times$ DW2 = [1, -2] $\times$ [1, +2] $\rightarrow$ [2, 0] + [0, 4] = S0 + SPW4. The former interaction can in principle take place throughout the thermosphere since DE1 has a long vertical wavelength and therefore can propagate to great heights, and DW1 can take the form of either diurnal winds driven by EUV forcing, or the diurnal variation of ion drag.

Figure 8 illustrates the latvsdoy depictions of zonal and meridional wind amplitudes for MIGHTI and CTMT S0 at 106 km and 250 km, analogous to the depictions presented previously for SE2 in Figure 2. For both u and v, at 106 km the main activity occurs around DOY 60-120 and DOY 240-330, with equatorial maxima present for v and absent for u. The absence of any significant equatorial-region maxima for u at 106 km is consistent with the absence of any equatorial maxima for u among all four HMEs characterized in Table 1. Also noteworthy is that the latvsdoy structures at 250 km do not correlate well with those at 106 km, except that the v structures near the equator at 250 km appear to be vertical projections of those at 106 km. For both u and v, The corresponding plots for the CTMT at 106 km show a striking correspondence with the MIGHTI results in Figure 8. However, contrary to MIGHTI, the CTMT results at 250 km correlate with those at 106 km, except interestingly, the one point of disagreement is that equatorial-region v structures at 250 km do not correlate well with the 106 km maxima within DOY 60-120 and DOY 240-330. To assist in understanding the reasons for these similarities and differences, we now turn to the htvslat and htvsdoy structures.

Recall that the first glimpse of S0 was provided in the right panels of Figure 6, but not discussed in connection with SE2 at that time. The S0 41dm amp/phz structures for u in Figure 6 stand in contrast to those shown in Figure 6 for SE2. Whereas the SE2 amp/phz structures are clearly consistent with the vertical propagation of a tide from below, with a single lower-thermosphere peak and downward phase progression, the S0 phase structure shows no evidence of a phase progression with height. Moreover, there are no HMEs that have u maxima near 18-24° latitude and peaks between 130 km and 220 km. A tentative conclusion that can be drawn is that for the 60 days centered on DOY 340, S0 is excited in-situ in the thermosphere. The CTMT S0 amp/phz structures in Figure S6-CTMT, with the response confined almost totally to poleward of 24°N and below 150 km, do not resemble those in Figure 6.

Additional insights into possible in-situ generation of S0 is provided in Figure 9, which is the analog of Figure 7 for SE2, and thus provides htvsdoy depictions at 0° and 30° latitude as well as select vertical profiles. The left panels include an additional set of amp/phz profiles for u at 18° latitude, except in this case for DOY 60. These profiles indicate a single main peak around 150-160 km, and above about 115 km the phases progress to later times with altitude. This phase progression with height is opposite to that expected for an upward-propagating wave, and may represent the presence of in-situ forcing. In addition, the htvsdoy amplitudes at 18°N for the CTMT (Figure S9-CTMT) are about one-fifth those for MIGHTI, and for all practical purposes negligible. This is consistent with the fact that the CTMT does not include in-situ sources.

The remaining panels in Figure 9 illustrate htvsdoy amp/phz structures for S0 v at 30° latitude (top, center) and 0° latitude (top, right), and amp/phz profiles for v at 27° latitude for DOY 330, and 0° latitude for DOY 90 and 300 (along the bottom row). The v amplitude profile for 27° latitude has a major peak (13 ms^{-1}) at about 145 km, and steady decrease in phase with height consistent with an average vertical wavelength of order 180 km. These characteristics are broadly consistent with that of HME2 for S0 (Table 1), yet the rate of decrease in amplitude with height above the peak is more indicative of HME3 than HME2. The v vertical phase profiles for DOY 90 and 300 at the equator also indicate vertical propagation from below, transitioning from vertical wavelengths of order 50 km below 145 km to much longer vertical wavelengths at higher heights, accompanied by major amplitude peaks around 115 km and 190-200 km and a secondary maximum in-between. It is not possible to ascertain from the data whether there are in-situ contributions to the two peaks above 145 km. These profile characteristics are consistent with the superposition of a high-order antisymmetric HME (e.g., HME3) with a low-order antisymmetric HME (e.g., HME1), both of which have primary or secondary latitudinal maxima at the equator. In the case of HME3, the secondary latitudinal peak at the equator is nearly the same magnitude as the primary latitudinal peaks at ±42°. The htvsdoy structures for the CTMT (Figure S9-CTMT) also show maxima in the 110-160 km height range, and in particular for v, penetration to altitudes above 200 km; these characteristics point to the presence of low-order HMEs. However, given the excellent match between MIGHTI and CTMT latvsdoy structures at 106 km shown in Figure 8, yet the differences in latvsdoy structures at 250 km, combined with the differences in htvsdoy structures between Figures 9 and S9-CTMT, one can reasonably conclude that some of these differences may be accounted for by in-situ sources for S0.

Figure 10 provides an additional view of S0, in this case 41dm htvslat depictions of amp/phz for u (left) and v (right) for DOY 125. The v profile for 27° latitude is similar to that discussed above for 27° for DOY 330 in that the peak also lies near 145 km. However, the amplitude decrease with height is also much greater than that of HME2 (normalized here to MIGHTI amp/phzs), which is illustrated in this figure as a red dashed line. Nevertheless, the phase profile is in excellent agreement with that of HME2. The htvslat structure of v in Figure 10 places the latitudinal maximum near 30°, which is also consistent with HME2. However, HME2 is zero at the equator, whereas equatorial values of order 4 ms^{-1} are evident in the MIGHTI data, which implies the presence of HME1 and/or HME3. We note that the latitudinal maximum for HME2 broadens to 42° near 200 km, which is the value given in Table 1. The upward tilt of the MIGHTI constant-amplitude contours from 18-24° latitude to 39° latitude is consistent with this behavior. Recall that one effect of molecular dissipation is that height structures vary with latitude, or equivalently, latitude structures vary with height, and this is what is revealed in the MIGHTI amplitudes, while the changes in phase structures are less severe. It is tentatively concluded that the mismatch between the MIGHTI amplitude decrease with height above 145 km at 27° latitude and that indicated by HME2 (red dashed line) (a) reflects an insufficiency in the way that HME2 has captured the change in latitude structure with height due to molecular dissipation, and/or (b) interferences between the height-latitude structures of HME1 and/or HME3 with that of HME2.

The htvslat structure for u in Figure 10 has a main peak near 27° latitude and 115 km altitude with downward phase progression, which suggests a high-order upward-propagating mode, perhaps beyond HME4. The maxima equatorward of 12° and below 145 km are associated with upward phase progression, contrary to upward propagation, and therefore not likely associated with the main peak at 27°. Furthermore, the increasing amplitudes between 200-280 km between 18° and 39°, without any associated phase progression, cannot be associated with the low-altitude main peak, and must reflect the response to an in-situ source.

It appears that the similarities in latvsdoy structures between MIGHTI and CTMT at 106 km that were noted in Figures 8 and S8-CTMT must mainly reflect higher-order

HMEs (i.e., HME3 and HME4) whose influence at higher altitudes in the htvslat plane give way to lower-order HMEs which are not as consistently expressed between MIGHTI and CTMT, and which give rise to greater differences between MIGHTI and CTMT at higher altitudes. This, combined with in-situ generated components inferred to be present in MIGHTI measurements, which are not present in the CTMT, result in the different latvsdoy structures between MIGHTI in Figure 8 and CTMT in Figure S8-CTMT at 250 km.

3.3 SW4

As noted in the previous subsection, several of the excitation mechanisms that produce S0 also produce SW4. SW4 is another semidiurnal tidal component that has not received much attention in the literature, although SW4 density perturbation is shown to compare quite well between CTMT and CHAMP (see Supporting Information to Oberheide et al., 2011a). Yet, as indicated in Figure 11, it is well expressed in the 61dm MIGHTI tides. During DOY 0-60 the u amplitude at 106 km peaks near 27° latitude (7-11 ms^{-1}) with values of order 5 ms^{-1} at the equator. From Table 1 this suggests the presence of HME2 (maximum at 30° latitude, zero amplitude at the equator) with secondary contributions from HME1 (maximum at the equator). The v component peaks near 24-36° latitude (consistent with both HME2 and HME1), with some evidence for a secondary maximum near the equator (consistent with HME2), and therefore fits with this interpretation of u. Similar maxima appear in the CTMT, also confined to the DOY 300-060 time period, and with similar magnitudes. At 250 km, the CTMT u and v maxima shift equatorward in a way that indicates dominance of HME1, consistent with the longer vertical wavelength of HME1 compared with HME2. However, the u and v maxima are 38% and 25% of their 106 km counterparts, as compared with 52% and 57% for ICON/MIGHTI. Given the importance of HME1 to the overall structures of the MIGHTI and CTMT depictions of SW4, a significant fraction of these percent differences may originate from the different levels of solar activity embodied in CTMT versus MIGHTI.

Figure 12 presents the htvslat plots for 61dm SW4 u and v for DOY 60. Also highlighted are the amp/phz vertical profiles for u at 0° latitude and for v at 18° latitude. Focusing on the un-smoothed black profile for u at 0° latitude, the major peak (18 ms^{-1}) occurs at about 118 km, consistent with that of HME1 in Table 1. (It is notable that in this case the smoothed blue-line profile gives the false impression that the major peak occurs near 140 km, as reflected in the htvslat color plot.) In addition, the HME1 vertical profile for u at 0° (red dashed line) predicts that the amplitudes at 160 km and 220 km that would be consistent with the 18 ms^{-1} peak at 118 km are 12 ms^{-1} and 9 ms^{-1}, respectively, as compared with 10 ms^{-1} and 6 ms^{-1} and for the corresponding black profile in Figure 12. At 118 km the latitudinal width at half-maximum is 39° latitude, which is consistent with the 33° half-width depicted in Figure 12. The corresponding phase profile at the equator (lower left panel) is also in excellent agreement with that of HME1. Note that the u phases are nearly constant with latitude, except at the higher altitudes and between 15-39° latitude. These phase departures from expectations for sole presence of HME1, as well as the differences in latitudinal half-width mentioned above, could in principle be due to some contribution from HME2 (which maximizes at 30° latitude). Therefore we conclude that the amp/phz structures for u in Figure 12 are dominated by HME1, with some possible contributions from HME2.

The right side of Figure 12 illustrates the htvslat distributions of SW4 v amp/phzs for DOY 60, and corresponding vertical amp/phz profiles at 18° latitude. A prominent amplitude peak occurs near 160 km altitude between 15° and 30° latitude. Within this latitude range there is also a secondary peak between 15-21° at 115 km that shifts downward to about 107 km between 24-33° latitude. The htvslat phase structure for v is also much more complicated than for u, showing an abrupt shift near 12° latitude, and vertical wavelengths that generally change with latitude and height throughout the domain. All of these features are consistent with interference between two or more HMEs, and are complicated by the fact that HME2 for v has near-equal maxima at the equator and 36° latitude, and HME1 for v has a maximum at 24° latitude (see Table 1). It is not productive or credible to speculate too much on every detail, but it is worth focusing on a few facts regarding the behavior of SW4 meridional wind amp/phzs in Figure 12. First, the vertical amp/phz profiles at 18° latitude on the right side of Figure 12 have superimposed (red dashed lines) the v amp/phzs that are predicted self-consistently (that is, applying the relative amp/phzs between u and v) from the HME1 u amp/phz profiles shown at the equator on the left of Figure 12. With the exception of the bite-out between 100-150 km, the measured and predicted amplitudes agree quite well above 150 km, and the phases agree at all heights. These facts are consistent with the strong presence of HME1. Second, the sharp phase transition around 12° in the htvslat plot for v is consistent with the presence of HME2, which has a considerably shorter vertical wavelength than HME1 and is therefore of secondary importance to HME1 at the higher altitudes. Notably, the measured vertical wavelength for v below 130 km is 45 km, consistent with HME2 (see Table 1). These facts are consistent with our interpretation for u, namely that HME1 is dominant and contains some contributions from HME2. For v, the latitude structures of HME1 and HME2 are such that the influence of HME2, at least below 150 km, is more significant than for u. We conclude that the lower observed v amplitudes compared to that predicted for HME1 below 150 km at 18° latitude are consistent with interference between HME1 and HME2, and perhaps even contain contributions from HME3 and HME4, which have maxima at nearby latitudes (see Table 1). We do note that the agreement between observed v phases and that predicted solely on the basis of HME1 calibrated against u seem inconsistent with the disagreement in the amplitude profiles, but this is what the measurements show and the agreement may therefore be fortuitous.

The CTMT htvslat profiles consistent with Figure 12 (see Figure S12-CTMT) are much less structured than the MIGHTI determinations, with u maximum at 110 km around 30°S, and with v maximum at 115 km near 15° latitude. The latter is consistent with HME3, and the former with HME2. There are also features in both u and v below 110 km that suggest the presence of HME3. The importance of HME3 in the CTMT, with its short vertical wavelength, also helps to explain the reduced amplitudes at 250 km relative to MIGHTI (where longer-wavelength HME1 plays an important role) that were discussed in connection with Figure 11. In general, the MIGHTI results for DOY 60 are not consistent with tidal climatology as expressed in the CTMT.

The differences in vertical structure between MIGHTI and CTMT are further illustrated and emphasized through comparison between the left two panels of Figures 13 and S13-CTMT, which depict the htvsdoy variability of SW4 amp/phzs at 6$\circ$ and 24° latitude. We first note a significant degree of agreement between MIGHTI and CTMT in terms of the greatly reduced amplitudes between about DOY 120 and DOY 300 at all altitudes, as compare with NH winter months. A notable difference is the existence of maxima around 140-160 km in the MIGHT amplitudes in addition to those at about 110 km, relative to the absence of the higher-altitude maxima in the CTMT. Also, although the lower-altitude maxima have similar amplitudes between MIGHTI and the CTMT, the amplitudes above about 200 km are much less in the CTMT than in MIGHTI. All of these facts are consistent with the greater presence of low-order HMEs in the MIGHTI observations than in the CTMT, consistent with the conclusions drawn above. And, although there are hints of separate maxima above about 220 km in the htvsdoy depictions in Figure 13, it is noted from the vertical profiles at the bottom of Figure 13 that there are significant uncertainties that are attached to these amplitudes. Moreover, there are no strong potential in-situ sources of SW4 in the middle and upper thermosphere. There we conclude that there is no evidence for in-situ sources of SW4 in the MIGHTI data.

3.4 SW1

Similar to the SW6,SE2 and SW4,S0 pairs generated through interaction of SW2 with stationary SPW4,SPW2 features, respectively, the SW3,SW1 pair arises through interaction of SW2 with stationary features representable as SPW1: SPW1 $\times$ SW2 = $[0, +1] \times [2, +2] \rightarrow [2, +3] + [2, +1]$ = SW3 + SW1. This interaction was first suggested by Forbes et al. (1995) to explain the existence of large SW1 tidal winds over South Pole (Hernandez et al., 1993; Forbes et al., 1995), and later examined in modeling (Yamashita et al. 2002; Angelats i Coll and Forbes, 2002; Liu and Roble, 2002) and UARS measurements (Angelats i Coll and Forbes 2002; Forbes and Wu, 2006) along with SW3. Subsequent modeling and observational efforts focused on the ionospheric consequences of SW1 in connection with large SPW1 occurrences during Northern Hemisphere (NH) winter, especially during stratosphere sudden warming events (Liu et al., 2010; Liu and Richmond, 2013; Maute et al., 2014; Pedatella and Forbes, 2010; Pedatella and Liu, 2013; see also review by Forbes, 2021). As noted in the modeling work of Jones et a., (2013), SW1 and SW3 can be generated in-situ in the thermosphere (especially during solar maximum), where SPW1 takes the form of zonal variations of ion drag due to the latitudinal displacement of Earth's magnetic field in the geographic coordinate system.

Figure 14 illustrates the latvsdoy distributions of u and v amplitudes of SW1 at 106 km and 250 km. The v component at 106 km has very specific signatures, maximizing during NH winter (DOY 300-060) with maxima near 6° latitude and $\gtrsim$30°. The u amplitude distribution also consists of higher and lower latitude bands of maxima, but somewhat less well-defined than for v, and with the lower-latitude maxima smaller than near 36°. The noteworthy feature of the SW1 amplitudes at 250 km is the maximum in v that occurs between DOY 120-240 and 6-12° with comparatively high amplitudes (5-8 ms^{-1}), and during a time of minimum SW1 activity at 106 km. This may be a signature of in-situ forcing, which is explored further below. The CTMT also exhibits a dual-band structure for v amplitudes, but the u response is confined to poleward of 24° latitude. The CTMT u and v amplitudes at 250 km are considerably reduced in amplitude compared to 106 km and the MIGHTI results at 250 km, which is suggestive of an SW1 component generated in-situ. The 4 HMEs for SW1 all have latitudinally-broad u and v maxima near 110 km at or near the poles (see Table 1), so the u and v amplitude signatures seen in the vicinity of 36°N at 106 km for both CTMT and MIGHTI are most likely linked to equatorward intrusions of those high-latitude maxima. For u there were no fits at 106 km and 250 km that passed the "veracity test" (as defined in Section 2.2) over a significant range of latitudes. Therefore only SW1 results for the v component are discussed in the following.

The SW1 peak in v amplitude at between DOY 120-240 at 250 km altitude is now explored further. That feature is also evident in the htvsdoy depiction at 6° latitude in the upper right-hand panel of Figure 13, and in the amplitude vertical profile in the lower right which shows significant scatter below 190 km. The phase profiles are consistent with downward phase progression (upward propagation) with very long vertical wavelength ($>$ 300 km) above 130 km, and much shorter vertical wavelength $\sim$35 km at lower altitudes. This picture is supplemented by the 61dm htvslat and amp/phz plots in the left side of Figure 15 for DOY 240, and the accompanying amp/phz vertical profiles for 9° latitude to the far left. Superposed on the MIGHTI amp/phz profiles are those for SW1 HME3 (calibrated to best fit the MIGHTI amp/phzs below 160km), which agree every well with the MIGHTI results at all altitudes for phase, and fall within the scattered MIGHTI amplitudes below 190 km. HME3 has a maximum at 18°, also consistent with the htvslat maximum ay 15° latitude and 130 km; we attribute the mismatch in altitude of maximum in the MIGHTI result versus the HME to the large amplitude uncertainties that are depicted. Above 190 km, there is a major departure between the observed amplitudes and the much smaller HME3 amplitudes in the profile plot. And, there are no low-order SW1 HMEs whose amplitudes increase with height above 190 km (cf. HME1 for SE2 v in Figure 4), or have maxima near 6-18° latitude at these altitudes. We therefore conclude that the SW1 maximum in v between 3-21° latitude and DOY 120-240 above 190 km results from in-situ excitation.

Another clear example of in-situ excitation of SW1 is shown in the right-hand panels of Figure 15, which include 41dm htvslat amp/phz depictions of v amplitude centered on DOY 0. Amplitudes of order 10 ms^{-1} above 160 km are seen in the vicinity of 36° latitude, without any evidence of phase progression consistent with upward wave propagation. The vertical amp/phz profiles at 36° latitude to the right confirm this. Moreover, none of the CTMT results in Figures S13-CTMT, S14-CTMT and S15-CTMT show any resemblance to the figures discussed above, which is also consistent with this interpretation.

3.5 SW2

It has been known for a long time (e.g., Butler and Small, 1963) that the dominant source of excitation of SW2 in the lower and middle thermosphere is heating resulting from the absorption of ultraviolet radiation by ozone, peaking around 45 km (Forbes and Garrett, 1978). Additional excitation of the semidiurnal tide occurs in the thermosphere through absorption of extreme ultraviolet radiation, and through the nonlinear interaction between the DW1 component of neutral winds and the DW1 component of ion drag: DW1 $\times$ DW1 $= [1, +1] \times [1, +1] \rightarrow [2, 2] + [0, 0] =$ SW2 + SPW0. Little work has been done in sorting out the relative importance of these sources. Forbes (1982) performed limited model calculations demonstrating that all 3 sources were of equal importance in accounting for semidiurnal variations in exospheric temperature under average solar conditions at 42°N. Forbes et al. (2011) performed HME fitting to TIMED/SABER semidiurnal tidal temperatures in the 100-110 km region, extrapolated the HMEs upwards in a manner similar to that performed within the CTMT, and on the basis of comparisons with semidiurnal exospheric temperatures derived from the CHAMP and GRACE satellites, concluded that nearly all of the semidiurnal variation is excited in-situ. The CHAMP and GRACE data were obtained in the 400-500 km height regime during 2004 and 2006, and may not be representative of the responses observed in the winds near 250 km at solar minimum that are the focus of the present study.

Latvsdoy depictions of u (left) and v (right) SW2 amplitudes from MIGHTI(CTMT) measurements at 106 km and 250 km are presented in the top(bottom) two rows of Figure 16. Note that the MIGHTI amplitudes are quite large, approaching 30 ms^{-1} at some latitudes/DOY at both altitudes. Similar to other semidiurnal tidal components, the MIGHTI latvsdoy structures are similar to climatology as expressed in the CTMT at 106 km. The notable features are that the smallest(largest) u amplitudes occur equatorward(poleward) of 12°N and throughout the year, while v amplitudes occur in 2 bands equatorward and poleward of about 18°N and mainly confined to DOY 120-270. However, at 250 km the CTMT structures do not mirror those of MIGHTI, and are generally smaller in amplitude by about 25% (v) and 40% (u). This is consistent with existence of an in-situ generated component.

Since HWM14 incorporates HRDI and WINDII winds (see also Emmert et al., 2002) with good local time coverage in the vicinity of 106 km and 250 km, comparisons are also made in Figure S16-HWM14 in Supporting Information between MIGHTI and HWM14 u and v SW2 winds. HWM14 reflects the same salient seasonal-latitudinal patterns in u and v as MIGHTI and the CTMT at 106 km. At 250 km, the u patterns are similar, with maxima occurring equatorward of about 24-30°N with small amplitudes during NH summer, i.e., DOY 120-240. However, the HWM14 u maxima are roughly a factor of two larger than those in the MIGHTI seasonal-latitudinal pattern, and the v patterns are completely different and to a significant degree visually anti-correlated. One contributing factor to these differences could be the difference in mean solar flux conditions between the WINDII red-line measurements near 250 km (mean F10.7 $\sim$ 115) in contrast to those of MIGHTI during 2020 (mean F10.7 $\sim$75), which would manifest in the HWM14 amplitudes if there is a significant SW2 in-situ component. Other potential contributing factors include differences in propagation conditions that would primarily affect long-wavelength tidal modes, and inter-annnual variability in the mixture of modes between the two data sets.

3.6 SW3

As noted in subsection 3.4, through the same mechanisms that generate SW1, SW3 can arise from troposphere heating, from SW2 modulation by SPW1 in the stratosphere-mesosphere, or in-situ in the thermosphere. The latvsdoy depictions of SW3 amplitudes at 106 km and 250 km are provided in Figure 17. At 106 km, maxima are of order 5-7 ms^{-1}, of similar order or greater than the other semidiurnal tides considered so far with the except of SW2. CTMT amplitude maxima are of order 7-8 ms^{-1} (see Figure S17-CTMT) with similar seasonal-latitudinal patterns as MIGHTI, except that the CTMT u and v amplitudes exhibit a precipitous drop-out during DOY 300-360 that is only present in MIGHTI during DOY 0-30. This may be evidence of inter-annual variability. It is noteworthy that the MIGHTI amplitudes at 250 km are slightly larger than those at 106 km, whereas for CTMT the 250 km amplitudes are generally less than half those at 106 km.

We interpret these differences as potential evidence of in-situ forcing of SW3 in the thermosphere.

The htvslat profiles of 61dm u and v for SW3 centered on DOY 90 are shown in Figure 18. These are supplemented by vertical amp/phz profiles of u at 9° latitude (left) and vertical amp/phz profiles of v at 0° and 27° latitude (right). Both u and v show changes in amp/phz structures with latitude that suggest the presence of more than one HME, and secondary maxima at high altitude that suggest the presence of responses to an in-situ source. HME1 for u has a latitudinally-broad structure (±30°) centered on the equator with long vertical wavelength, and thus the MIGHTI structure appears to be dominated by HME1. This is confirmed by the reasonable match between the red dashed curves and the MIGHTI profiles at 9° latitude that are depicted in Figure 18, although the altitude of maximum u amplitude is distinctly lower than that of MIGHTI. In principle this altitude mismatch could be due in part to interference with HME3, which also has a u maximum at the equator (see Table 1), but may also reflect shortcomings in the calculated HME structure itself.

For v, HME1 and HME3 have zero amplitude at the equator, so HME2 is a good candidate to investigate. Indeed, the amp/phz profiles for v at 0° to the right in Figure 18 provide a reasonable approximation to the MIGHTI data, except that that are no HMEs that would be consistent with the increase in amplitude seen above 190 km. This provides additional evidence of a potential in-situ source. In the case of the v amp/phz profiles at 27° latitude shown in Figure 18, it is likely that HME1 (latitude maximum at 24°) and HME2 (latitude maximum at 36°) are both contributing, so no attempt is made there to compare with a single theoretical HME structure.

Figure 19 provides additional insights in the form of SW3 htvsdoy depictions for u at 6° and 18° latitude, and v at 30° latitude. The u amplitude structures around DOY 120 also suggest an in-situ source, since all HMEs for SW3 reflect a decrease in amplitude above 150 km, whereas those depicted in Figure 19 (see also vertical profiles in the bottom row) show a structure that is slightly increasing or constant above 150 km. Therefore, we conclude that the MIGHTI data above 150 km appear to be consistent with the presence of an in-situ source, but one that is weaker than for its partner wave, SW1.

3.7 Longitudinal dependence of the total semidiurnal tide

A final point to be made concerns the aggregate contributions of the non-migrating semidiurnal tides SE2, S0, SW1, SW3, SW4 to the longitudinal variation of the total semidiurnal tide (that is, also including SW2) at a given latitude. For example, Figure 20 depicts the lonvsdoy variability of u at 106 km (top) and v at 250 km (bottom) for the total semidiurnal tide at (left to right) 0°, 18° and 36° latitude. A similar plot for SW2 alone would be independent of longitude, but would reflect the DOY variation at each latitude according to Figure 16. The point is, that despite the relatively small amplitudes (4-8 ms^{-1}) of each nonmigrating component as illustrated in Figures 2, 8, 11, 14 and 17, the aggregation of these semidiurnal tides produces large longitudinal variability in the total semidiurnal tidal component. The illustrated longitude variability consists of a minimum to maximum ranges of order 15-25 ms^{-1} or 40-60% about mean values depending on DOY at both 106 km and 250 km. Since this longitudinal variability is representative of wind variability in the dynamo region, we can expect that some fraction of this variability will translate to the variability of the semidiurnal component of electric fields, $\mathbf{E} \times \mathbf{B}$ plasma drifts and electron density variations in the F-region ionosphere. Similarly, regarding the v component of the semidiurnal tide at 250 km, the displayed variability should produce measurable longitudinal variations in hmF2 and Ne through field-aligned transport (i.e., see Forbes et al., 2018).

4 Summary and Conclusions

It was explained in the Introduction how the combined effects of the $1/\rho$ dependence of viscosity, planetary rotation, ion drag and the λ_z and frequency of a tide are expected to determine its vertical and latitudinal structure as it propagates into and through a dissipative thermosphere; that in theory the height-latitude structure of any given tide can be approximated by the superposition of 2-4 HMEs, and as such can be quite complex; and, that observations that elucidate such structures in the thermosphere have been essentially absent.

In this paper daytime meridional and zonal wind measurements from the ICON/MIGHTI instrument are used to provide the first depictions of solar semidiurnal tidal structures in the 100 km to 280 km altitude region. The latitude (9°S-39°N) versus DOY variability of SE2, S0, SW1, SW2, SW3 and SW4 at 250 km are depicted for the first time, and evaluated in light of similar results at 106 km and the CTMT. Also revealed for the first time are the height versus latitude structures of SE2, S0, SW1, SW3 and SW4 centered on specific DOY, and their height versus DOY structures at select latitudes. The structures of SW2 were not reported due to concerns with aliasing from zonal mean winds. The CTMT, which does not include the responses to in-situ tidal excitation in the thermosphere, was also used to assist in interpretation of the results, as were the height versus latitude HME structures which are the basis functions for the CTMT.

The data analysis and comparisons with the CTMT and HMEs reveal the following:

1. The latvsdoy structures of MIGHTI S0, SW2, and SW4 at 106 km are generally well represented by the corresponding CTMT climatologies, whereas the latvsdoy distributions of SE2, SW1, and SW3 in the CTMT capture some but not all major features observed during 2020. In all cases, the MIGHTI and CTMT amplitudes at 106 km are of the same order, with maxima generally in the range of 4-8 ms^{-1}.
2. In general, the MIGHTI latvsdoy structures at 250 km are much different than those represented in the CTMT. In the case of S0, SW1 and SW3, this is due to the presence of in-situ-generated components in the MIGHTI tides which are not included in the CTMT. In all cases, the MIGHTI-CTMT discrepancies are connected with differences in low-order tides (i.e., those with long vertical wavelengths and few nodes in their latitudinal structures) which are more capable of propagating from 106 to 250 km. In part, low-order tides may not be consistently expressed in MIGHTI and CTMT at the lower heights, and the impacts of these inconsistencies grow with altitude. But other factors potentially at play include inadequacies in the modeling behind the computation of HMEs (e.g., specification of ion drag and the absence of mean wind effects), and effects related to differences in solar cycle (F10.7 = 110 for CTMT and $\approx$ 75 for ICON/MIGHTI data collected in 2020) which primarily impact the low-order tides.
3. The htvslat structures of SE2, S0, SW1, SW3 and SW4 are complex, due to the fact that they represent the superposition of two or more HMEs, making the contributions of each HME difficult to sort out. Nevertheless it was possible to interpret and explain many of the height-latitude tidal structures in terms of few

HMEs, thus underscoring their viability for such interpretations as well as our understanding of how a dissipative thermosphere affects semidiurnal tidal propagation across a range of vertical wavelengths. As one general and obvious example, it could be seen that the low-order HMEs with the longest vertical wavelengths dominate above about 160 km. This is consistent with the theory for vertically-propagating tides in a viscous atmosphere.

4. Although the individual amplitudes of the non-migrating tides SE2, S0, SW1, SW3 and SW4 are modest in comparison to SW2, their aggregate effect is to produce large variations in the total semidiurnal tide at a given latitude. The implication is that the revealed longitude variability at 106 km will measurably impact the longitude variability of electric fields, plasma drifts and Ne variations in the F-region; and that the longitude variability of meridional winds at 250 km is indicative of field-aligned drifts that will introduce additional Ne longitude variability vis-a-vis vertical motions of the F-layer.

Although much was learned in the present study, a broad conclusion that can be drawn is that we still do not fully understand all of the factors that determine the propagation of semidiurnal tides from the lower to middle and upper thermosphere, and that further investigations of semidiurnal tidal propagation above 100 km are warranted using models that contain more complete physics than the model used to generate HMEs. The present results will hopefully motivate and serve to validate such studies.

Acknowledgments

ICON is supported by NASA's Explorers Program through contracts NNG12FA45C and NNG12FA42I. The data utilized in this study are available at the ICON data center (https://icon.ssl.berkeley.edu/Data). The CTMT netCDF data files can be found at https://doi.org/10.5281/zenodo.5541913. JO acknowledges support through NASA grants 80NSSC19K0258 and 80NSSC20K1353.

References

[1] Angelats i Coll, M., & Forbes, J.M. (2002). Nonlinear interactions in the upper atmosphere: The s = 1 and s = 3 nonmigrating semidiurnal tides. *Journal of Geophysical Research: Space Physics, 107*, p. SIA 3-1-SIA 3-15.

doi:10.1029/2001JA900179

[2] Butler, S.T. & Small, K.A. (1963). The excitation of atmospheric oscillations. *Proc. Roy. Soc., A274*, 91–121.

[3] Chapman, S., & Lindzen, R.S. (1970). *Atmospheric Tides*, D. Reidel, Dordrecht, Holland.

[4] Cullens, C.Y., Immel, T.J., Triplett, C.C. et al. (2020) Sensitivity study for ICON tidal analysis. *Progress in Earth and Planetary Sciences, 7*:18. doi:10.1186/s40645-020-00330-6

[5] Drob, D.P., et al. (2015). An update to the Horizontal Wind Model (HWM): The quiet time thermosphere, *Earth and Space Science, 2*, 301–319. doi:10.1002/2014EA000089

[6] Englert, C.R., Harlander, J.M., Brown, C.M., Marr, K.D., Miller, I.J., Stump, J.E., Hancock, J., Peterson, J.Q., Kumler, J., Morrow, W.H., Mooney, T.A., Ellis, S., Mende, S.B., Harris, S.E., Stevens, M.H., Makela, J.J., Harding, B.J., & Immel, T.J. (2017). Michelson Interferometer for Global High-resolution Thermospheric Imaging (MIGHTI): instrument design and calibration. *Space Science Reviews, 212,* 553–584. https://10.1007/s11214-017-0358-4

[7] Forbes, J.M. (1982). Atmospheric tides. I. Model description and results for the solar diurnal component. *Journal of Geophysical Research: Space Physics, 87*, 5222–5240.

[8] Forbes, J.M. (2000). Wave coupling between the lower and upper atmosphere: Case study of an ultra-fast Kelvin wave. *Journal of Atmospheric and Solar-Terrestrial Physics, 62*, 1603–1621.

[9] Forbes, J.M. (2021). Atmosphere-Ionosphere (A-I) Coupling by Solar and Lunar Tides, *in Space Physics and Aeronomy, Volume 4, Upper Atmosphere Dynamics and Energetics*, Wenbin Wang (Editor), Yongliang Zhang (Editor-in-Chief), Larry J. Paxton (Editor-in-Chief), May 2021 American Geophysical Union 560 Pages, ISBN: 978-1-119-50756-7

[10] Forbes, J.M., & Garrett, H.B. (1976). Solar Diurnal Tide in the Thermosphere, *Journal of the Atmospheric Sciences, 33*, 2226–2241. doi:10.1175/1520-0469(1976)033¡2226:SDTITT¿2.0.CO;2

[11] Forbes, J.M., & Hagan, M.E. (1979). Tides in the joint presence of friction and rotation: An f-plane approximation. *Journal of Geophysical Research: Space*

Physics, 84, 803–810. doi:10.1029JA084iA03p00803.

[12] Forbes, J.M., & Hagan, M.E. (1982). Thermospheric extensions of the classical expansion functions for semidiurnal tides. *Journal of Geophysical Research: Space Physics, 87*, 5253–5259. doi:10.1029JA087iA07p05253.

[13] Forbes, J.M., Makarov, N.A., & Portnyagin, Y.I. (1995). First results from the meteor radar at South Pole: A large 12-hour oscillation with zonal wave number one. *Geophysical Research Letters, 22*, 3247–3250. doi:10.1029/95GL03370

[14] Forbes, J.M., & Wu, D. (2006). Solar tides as revealed by measurements of mesosphere temperature by the MLS experiment on UARS. *Journal of the Atmospheric Sciences, 63*, 1776–1797. doi:10.1175/JAS3724.1

[15] Forbes, J.M., Zhang, X., Bruinsma, S., & Oberheide, J. (2011). Sun-synchronous thermal tides in exosphere temperature from CHAMP and GRACE accelerometer measurements. *Journal of Geophysical Research: Space Physics, 116*, A11309. doi:10.1029/2011JA016855.

[16] Forbes, J.M., Maute, A., Zhang, X., & Hagan, M.E. (2018). Oscillation of the ionosphere at planetary-wave periods. *Journal of Geophysical Research: Space Physics, 123*, 7634–7649. https://doi.org/10.1029/2018JA025720

[17] Forbes, J.M., Zhang, X., Heelis, R., Stoneback, R., Englert, C.R., Harlander, J.M., et al. (2021). Atmosphere- Ionosphere (A-I) coupling as viewed by ICON: Day-to-day variability due to planetary wave (PW)-tide interactions. *Journal of Geophysical Research: Space Physics, 126*, e2020JA028927. doi:10.1029/2020JA028927

[18] Gasperini, F., Forbes, J.M., & Hagan, M.E. (2017). Wave coupling from the lower to the middle thermosphere: Effects of mean winds and dissipation. *Journal of Geophysical Research: Space Physics, 122*, 7781–7797. doi:10.1002/2017JA024317

[19] Hagan, M.E., & Forbes, J.M. (2003). Migrating and nonmigrating semidiurnal tides in the middle and upper atmosphere excited by tropospheric latent heat release. *Journal of Geophysical Research: Space Physics, 108,* 1062. https://doi.org/10.1029/2002JA009466

[20] Hagan, M.E., Maute, A., & Roble, R.G. (2009). Tropospheric tidal effects on the middle and upper atmosphere. *Journal of Geophysical Research: Space Physics, 114*, A01302. doi:10.1029/2008JA013637.

[21] Harding, B.J., Makela, J.J., Englert, C.R., Marr, K.D., Harlander, J.M., England, S.L. and Immel, T.J. (2017). The MIGHTI Wind Retrieval Algorithm: Description and Verification. *Space Science Reviews, 212,* 585–600. doi:10.1007/s11214-017-0359-3

[22] Harding, B.J., Chau, J.L., He, M., Englert, C.R., Harlander, J.M., Marr, K.D., et al. (2021). Validation of ICON-MIGHTI thermospheric wind observations: 2. Green-line comparisons to specular meteor radars. *Journal of Geophysical Research: Space Physics, 126,* e2020JA028947. doi:10.1029/2020JA028947

[23] Hernandez, G., Fraser, G.J., & Smith, R.W. (1993). Mesospheric 12-hour oscillation near the South Pole, Antarctica, *Geophysical Research Letters, 20*, 1787–1790. doi:10.1029/93GL01983

[24] Hong, S.-S., & Lindzen, R.S. (1976). Solar Semidiurnal Tide in the Thermosphere. *Journal of Atmospheric Sciences, 33*, 135–153. doi:10.1175/1520-0469(1976)033¡0135:SSTITT¿2.0.CO;2

[25] Jones Jr., M., Forbes, J.M., Hagan, M.E., & Maute, A. (2013). Non-migrating tides in the ionosphere-thermosphere: In situ versus tropospheric sources. *Journal of Geophysical Research: Space Physics, 118*, 2438–2451. doi:10.1002/jgra.50257

[26] Lindzen, R.S. (1968). Vertically propagating waves in an atmosphere with Newtonian cooling inversely proportional to density. *Canadian Journal of Physics, 46*, 1835–1840. doi:10.1139/p68-520

[27] Lindzen, R.S., Hong, S.-S., & Forbes, J.M. (1977). Semidiurnal Hough mode extensions in the thermosphere and their application. *Memorandum Report 3442*, Naval Research Laboratory, Washington, D.C.

[28] Liu, H.-L., & Richmond, A.D. (2013). Attribution of ionospheric vertical plasma drift perturbations to large-scale waves and the dependence on solar activity. *Journal of Geophysical Research: Space Physics, 118*, 2452–2465. doi:10.1002/jgra.50265

[29] Liu, H.-L., & Roble, R.G. (2002). A study of a self-generated stratospheric sudden warming and its mesospheric–lower thermospheric impacts using the coupled TIME-GCM/CCM3. *Journal of Geophysical Research: Space Physics, 107*, 4695. doi:10.1029/2001JD001533

[30] Liu, H.-L., Wang, W., Richmond, A.D., & Roble, R.G. (2010). Ionospheric variability due to planetary waves and tides for solar minimum conditions. *Journal of*

Geophysical Research: Space Physics, 115, A00G01. doi:10.1029/2009JA015188

[31] Makela, J.J., Baughman, M., Navarro, L.A., Harding, B.J., Englert, C.R., Harlander, J.M., et al. (2021). Validation of ICON-MIGHTI thermospheric wind observations: 1. Nighttime Red-line Ground-Based Fabry-Perot Interferometers. *Journal of Geophysical Research: Space Physics, 126*. doi:10.1029/2020JA028726

[32] Maute, A., Hagan, M.E., Richmond, A.D., & Roble, R.G. (2014). TIME-GCM study of the ionospheric equatorial vertical drift changes during the 2006 stratospheric sudden warming. *Journal of Geophysical Research: Space Physics, 119*, 1287–1305. doi:10.1002/2013JA019490

[33] Oberheide, J., Forbes, J.M., Häusler, K., Wu, Q., & Bruinsma, S.L. (2009). Tropospheric tides from 80 to 400 km: Propagation, interannual variability, and solar cycle effects.*Journal of Geophysical Research: Space Physics, 114*, D00I05. doi:10.1029/2009JD012388

[34] Oberheide, J., Forbes, J.M., Zhang, X., & Bruinsma, S.L. (2011a). Climatology of upward propagating diurnal and semidiurnal tides in the thermosphere. *Journal of Geophysical Research: Space Physics, 116*, A11306. doi:10.1029/2011JA016784

[35] Oberheide, J., Forbes, J.M., Zhang, X., & Bruinsma, S.L. (2011b), Wave-driven variability in the ionosphere- thermosphere-mesosphere system from TIMED observations: What contributes to the "wave 4"?, J. Geophys. Res., 116, A01306, doi:10.1029/2010JA015911.

[36] Pedatella, N.M., Hagan, M.E., & Maute, A. (2012). The comparative importance of DE3, SE2, and SPW4 on the generation of wavenumber-4 longitude structures in the low-latitude ionosphere during September equinox. *Geophysical Research Letters, 39*, L19108. doi:10.1029/2012GL053643.

[37] Pedatella, N.M., & Forbes, J.M. (2010). Evidence for stratosphere sudden warming-ionosphere coupling due to vertically propagating tides. *Geophysical Research Letters, 37*, L11104. doi:10.1029/2010GL043560

[38] Pedatella, N.M., & H.-L. Liu (2013), The influence of atmospheric tide and planetary wave variability during sudden stratosphere warmings on the low latitude ionosphere. *Journal of Geophysical Research: Space Physics, 118*, 5333–5347. doi:10.1002/jgra.50492

[39] Richmond, A.D. (1975). Energy relations of atmospheric tides and their significance to approximate methods of solution for tides with dissipative

forces, *Journal of the Atmospheric Sciences, 32*, 980–987. doi:10.1175/1520-0469(1975)032¡0980:EROATA¿2.0.CO;2

[40] Svoboda, A.A., Forbes, J.M., & Miyahara, S. (2005). A space-based climatology of diurnal MLT tidal winds, temperatures and densities from UARS wind measurements. *Journal of Atmospheric and Solar-Terrestrial Physics, 67*, 1533–1543.

[41] Truskowski, A.O., Forbes, J M., Zhang, X., & Palo, S.E. (2014). New perspectives on thermosphere tides—1. Lower thermosphere spectra and seasonal-latitudinal structures. *Earth, Planets and Space, 66*:136. doi:10.1186/s40623-014-0136-4

[42] Yamashita, K., Miyahara, S., Miyoshi, Y., Kawano, K., & Ninomiya, J. (2002). Seasonal variation of non-migrating semidiurnal tide in the polar MLT region in a general circulation model. *Journal of Atmospheric and Solar-Terrestrial Physics, 64*, 1083–1094. doi:10.1016/S1364-6826(02)00059-7

[43] Yanowitch, M. (1967). Effect of viscosity on gravity waves and the upper boundary condition. *Journal of Fluid Mechanics, 29*, 209–231. doi:10.1017/S002211206700076X

[44] Zhang X., Forbes, J.M., & Hagan, M.E. (2010a). Longitudinal variation of tides in the MLT region: 1. Tides driven by tropospheric net radiative heating. *Journal of Geophysical Research: Space Physics, 115*, A06316. doi:10.1029/2009JA014897

[45] Zhang X., Forbes, J.M., & Hagan, M.E. (2010b). Longitudinal variation of tides in the MLT region: 2. Relative effects of solar radiative and latent heating. *Journal of Geophysical Research: Space Physics, 115*, A06317. doi:10.1029/2009JA014898

Table 1. Height-latitude characteristics of semidiurnal HME zonal (u) and meridional (v) winds: Altitude z of maximum u amplitude to nearest 4 km, u vertical wavelength λ_z, and latitudes of u and v wind peaks (LatMax) at z. Asterisked(unasterisked) λ_z's are based on 102 km vs. 151 km (90 km vs. 110 km) phase differences. If the altitude of v maximum differs substantially from that of u, its height and/or latitude are given in parentheses; $\gtrsim$ means that amplitudes approach an asymptotic limit near this altitude. Latitudes/altitudes in italics indicate smaller, secondary peaks. HME1 and HME3 are symmetric, HME2 and HME4 are antisymmetric, except for S0 for which the order is reversed.

	HME1		**HME2**		**HME3**		**HME4**	
Tidal Component	z(km)/ λ_z(km)	LatMax(°) $(U;V)$	z(km)/ λ_z(km)	LatMax(°) $(U;V)$	z(km)/ λ_z(km)	LatMax(°) $(U;V)$	z(km)/ λ_z(km)	LatMax(°) $(U;V)$
SE2	213(247) /173*	0; (±36)	143/93*	±30; 0,±*60*	114/65*	*0*,±36; ±24,±*72*	114/44	±*12*,±42; ±*0*,±36,±*78*
S0	145($\gtrsim$200) /151*	±48; (0)	143($\gtrsim$200) /103*	±42; (±42)	114/81*	±*18*,±54; *0*,±42	110/46	±*18*,±54; ±*18*,±54
SW1	110(130) /137*	±90; (±*18*),±90	110/111*	±90; *0*,±90	110/67	±*18*,±90; ±72,±*18*	110/42	±*30*,±90; ±*0*,±*30*,±90
SW2	122/107*	±24; ±30	114/72*	±48; *0*,±48	110/45	*0*,±54; ±*18*,±54	110/33	±*24*,±60; *0*,±*24*,±60
SW3	122/81*	0; ±24	114/55	±36; *0*,±36	110/37	*0*,±48; ±*12*,±48	110/29	±*18*,±54; *0*,±*24*,±54
SW4	118/73	0; ±24	114/42	±30; *0*,±36	110/32	*0*,±42; ±*12*,±42	110/26	±*18*,±48; *0*,±*24*,±48

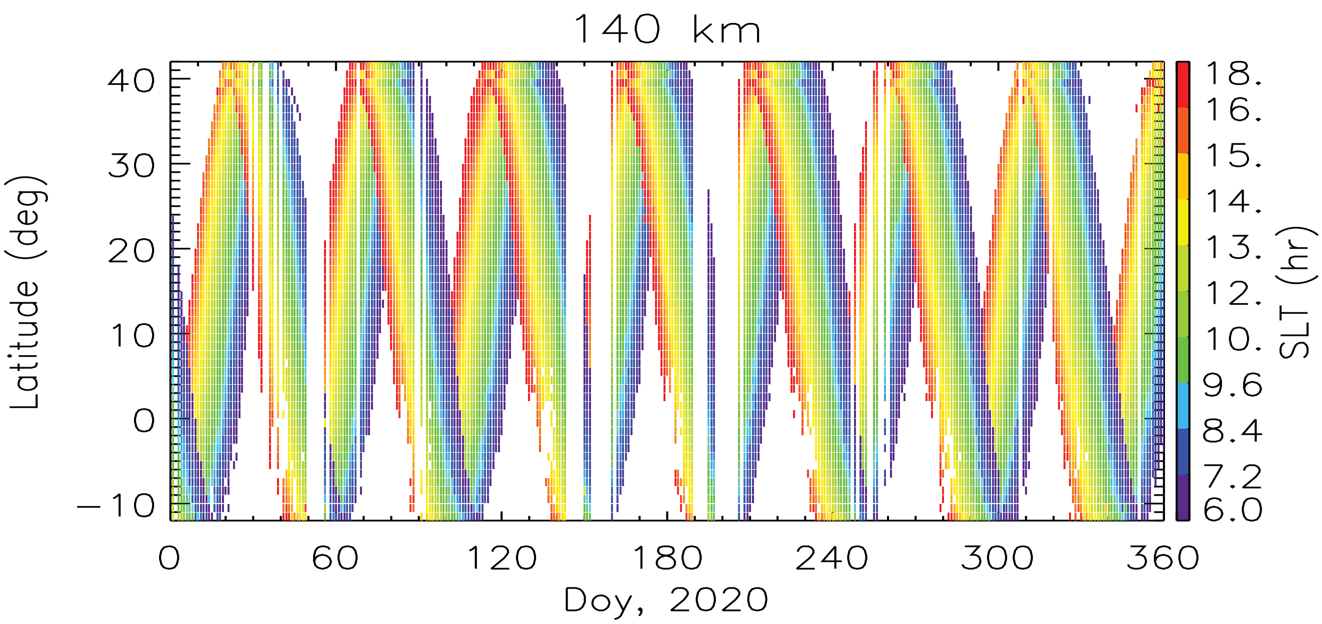

Figure 1. Solar local time coverage of MIGHTI wind measurements during daytime as a function of latitude and DOY, 2020, at 140 km. This coverage is typical of the wind data between 100 km and 280 km, which are used to extract semidiurnal tidal amplitudes and phases in this height range. Gaps mainly occur in connection with the SAA and other data quality considerations, and are taken into account by choosing appropriate windows within which tidal fitting is performed. See text for more details.

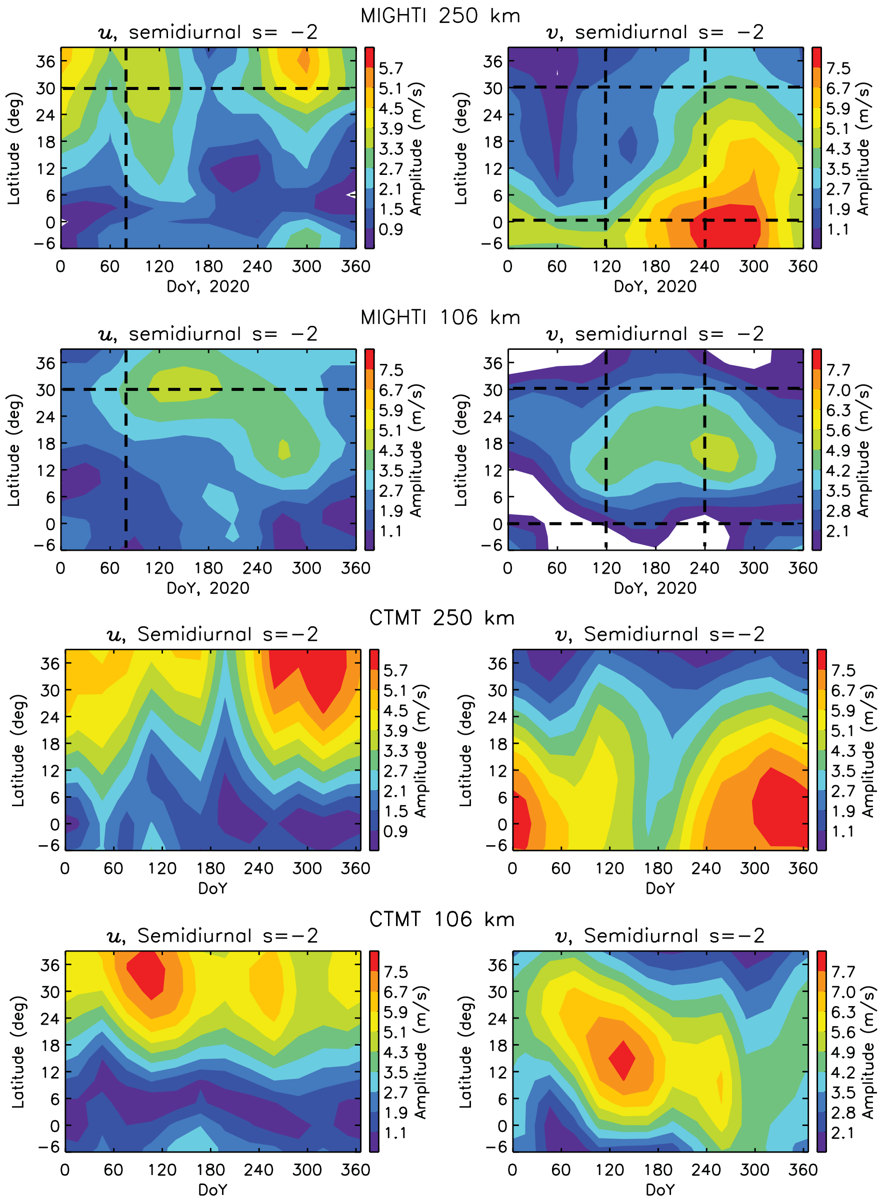

Figure 2. Top(bottom) 4 panels: Latvsdoy depictions of u (left) and v (right) amplitudes of SE2 from MIGHTI(CTMT) at 106 km and 250 km. The vertical(horizontal) dashed lines indicate DOY(latitude) of htvslat(htvsdoy) plots in Figures 5,6, and 7.

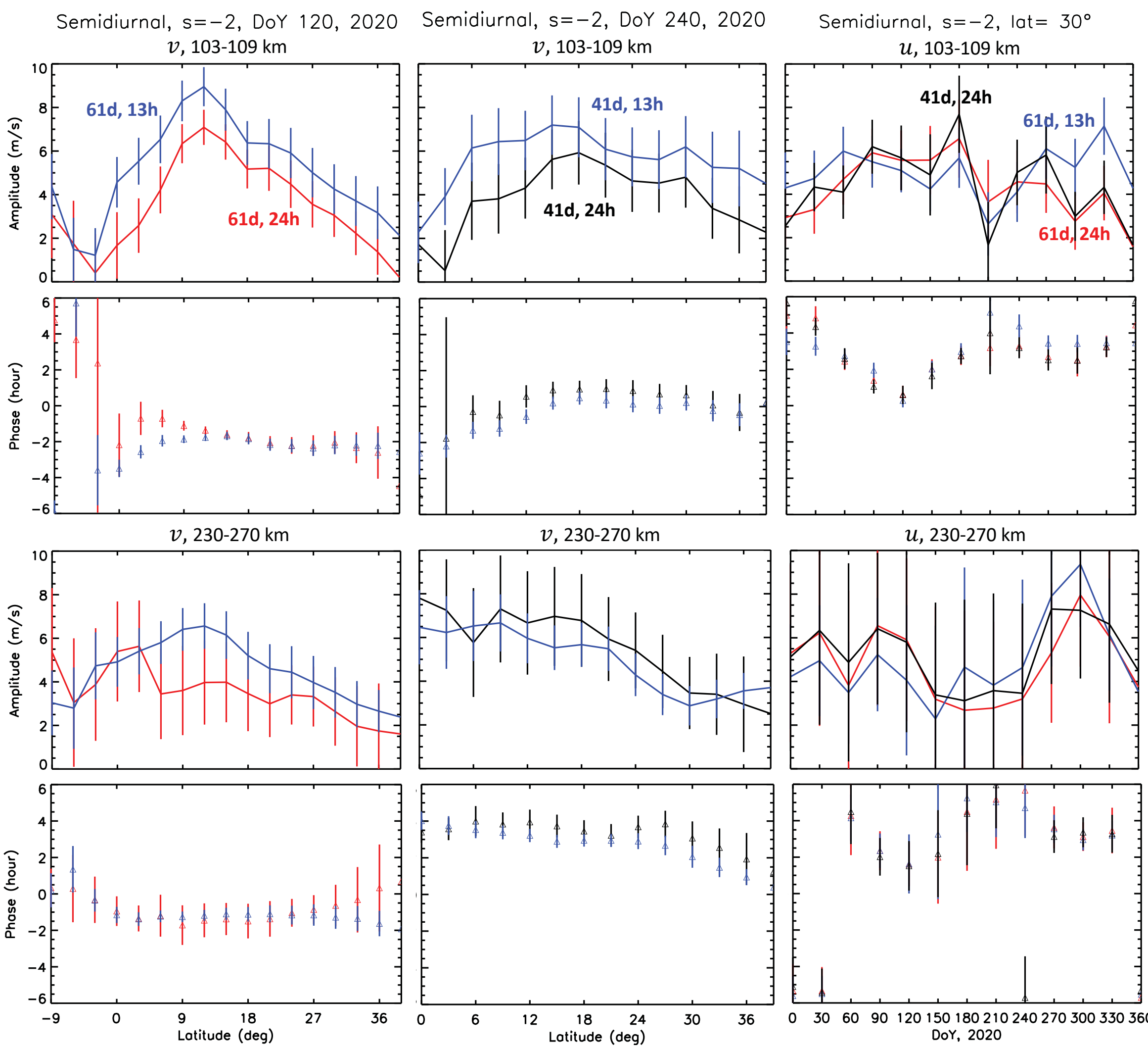

Figure 3. Comparisons between SE2 amplitudes and phases obtained by fitting data over 24h LST within 41d windows (black), over 24h LST within 61d windows (red), and over 13h LST within 41d or 61d windows as indicated (blue). The top(bottom) two rows depict amplitudes and phases at the mean heights of 106 km(250 km). Left: v versus latitude centered on DOY 120. Middle: v versus latitude centered on DOY 240. Right: u averaged over 30° ± 5° latitude versus DOY.

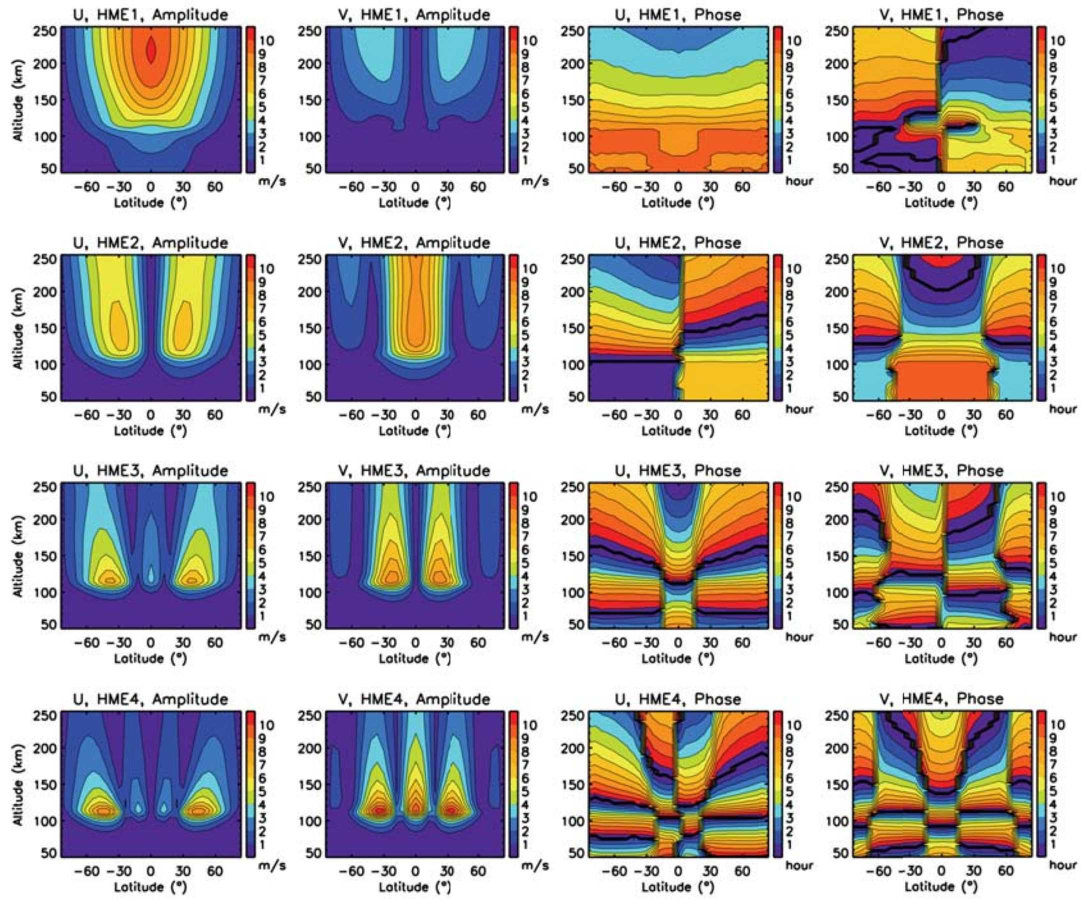

Figure 4. Htvslat depictions of amplitudes and phases for u and v corresponding to the first 4 HMEs of SE2. For each HME, u amplitudes are normalized to a maximum value of 8 ms^{-1}, and the phases are arbitrary. The v amplitudes and phases are self-consistent in a relative sense to those of U, as explained in some detail in the text. The phases depicted here for v are positive southward, consistent with the co-latitudinal coordinate system used in their computation, and with that of classical tidal theory (Chapman and Lindzen, 1970).

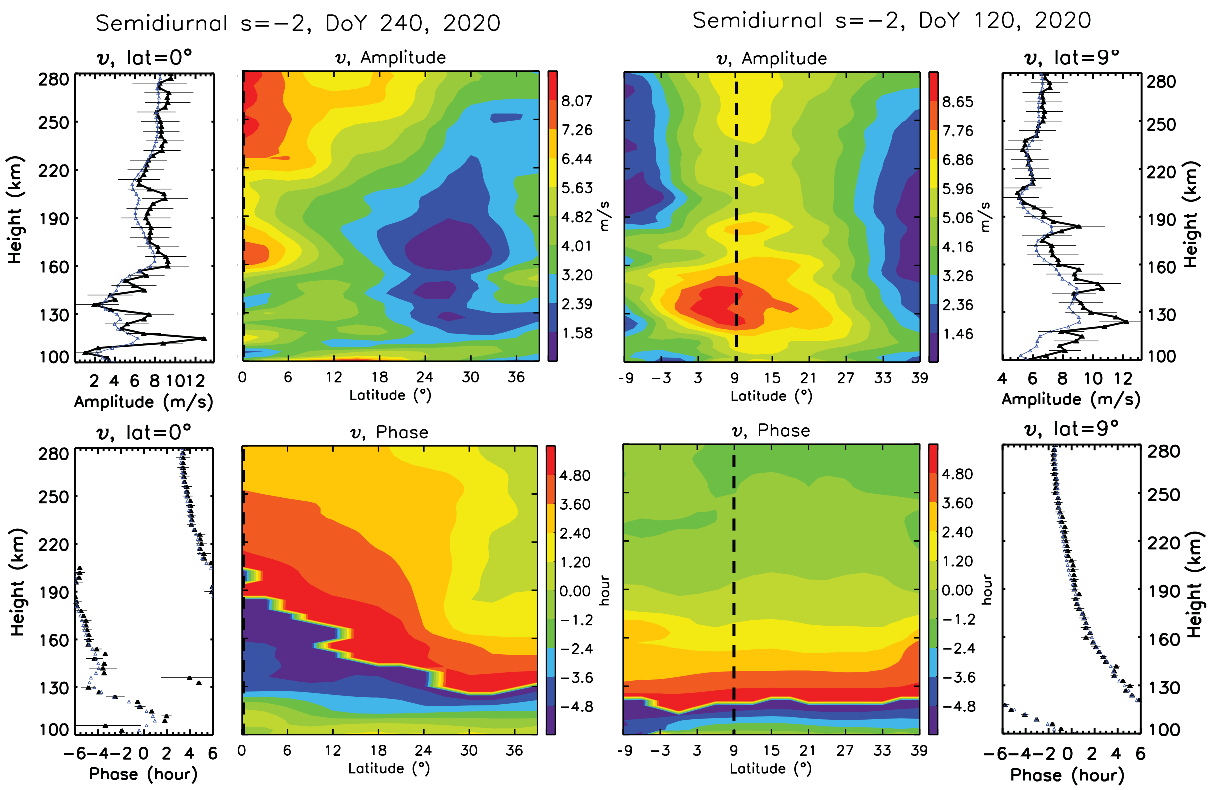

Figure 5. Depictions of SE2 amplitudes (top) and phases (bottom), in htvslat format, and in vertical profile format at fixed latitudes. Left: 41dm htvslat plots, and vertical profiles at 0° latitude, for v centered on DOY 240. Right: 61dm htvslat plots, and vertical profiles at 9° latitude, for v centered on DOY 120. The latitudes of the vertical dashed lines in the htvslat plots correspond to those of the vertical profiles. The black dots, lines and standard deviations in the vertical profile plots are calculated according to the methodology described in the text, and the blue symbols and lines in those figures represent the smoothed amp/phz structures that form the basis for the htvslat contour plots. Refer to dashed lines in Figure 2 for latvsdoy context of these SE2 plots at 106 km and 250 km.

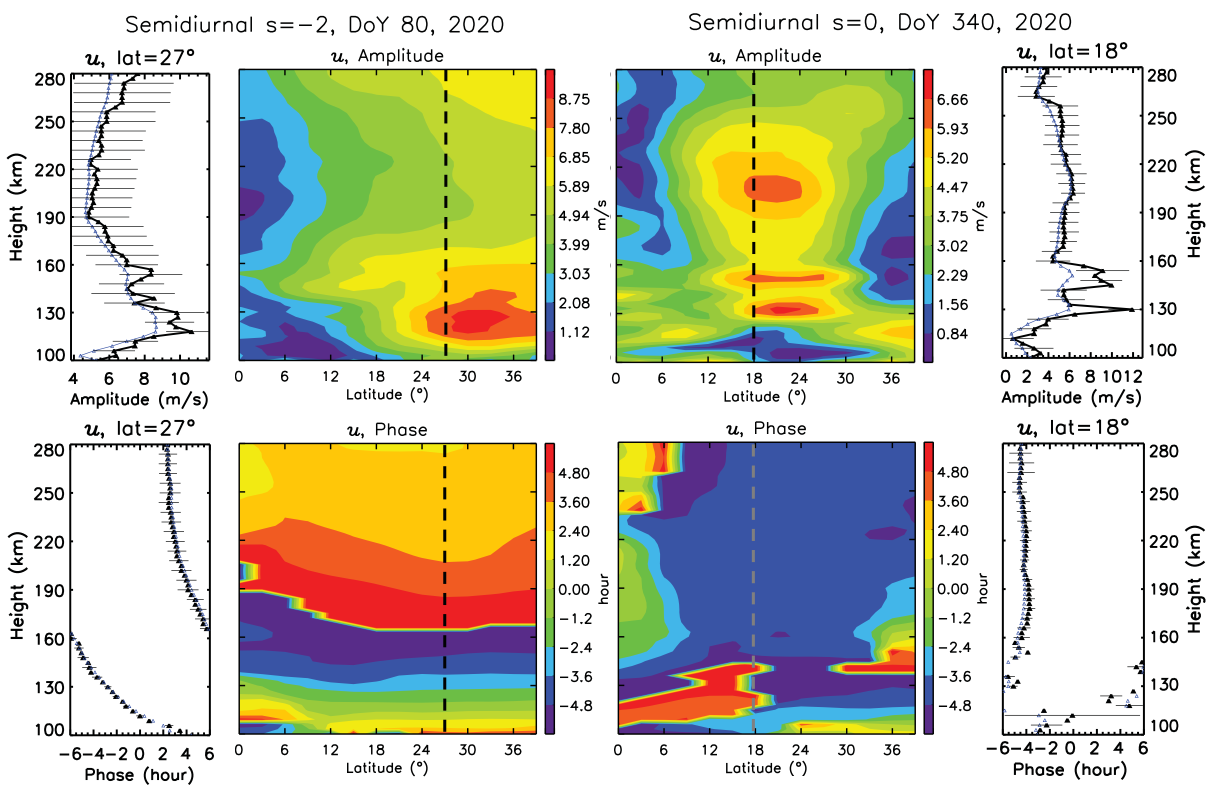

Figure 6. Same as Figure 5, except left: 41dm SE2 u centered on DOY 80, and profiles at 27° latitude, and right: 41dm S0 u centered on DOY 340, and profiles at 18° latitude. Refer to dashed lines in Figure 2(8) for latvsdoy context of the SE2(S0) plots at 106 km and 250 km.

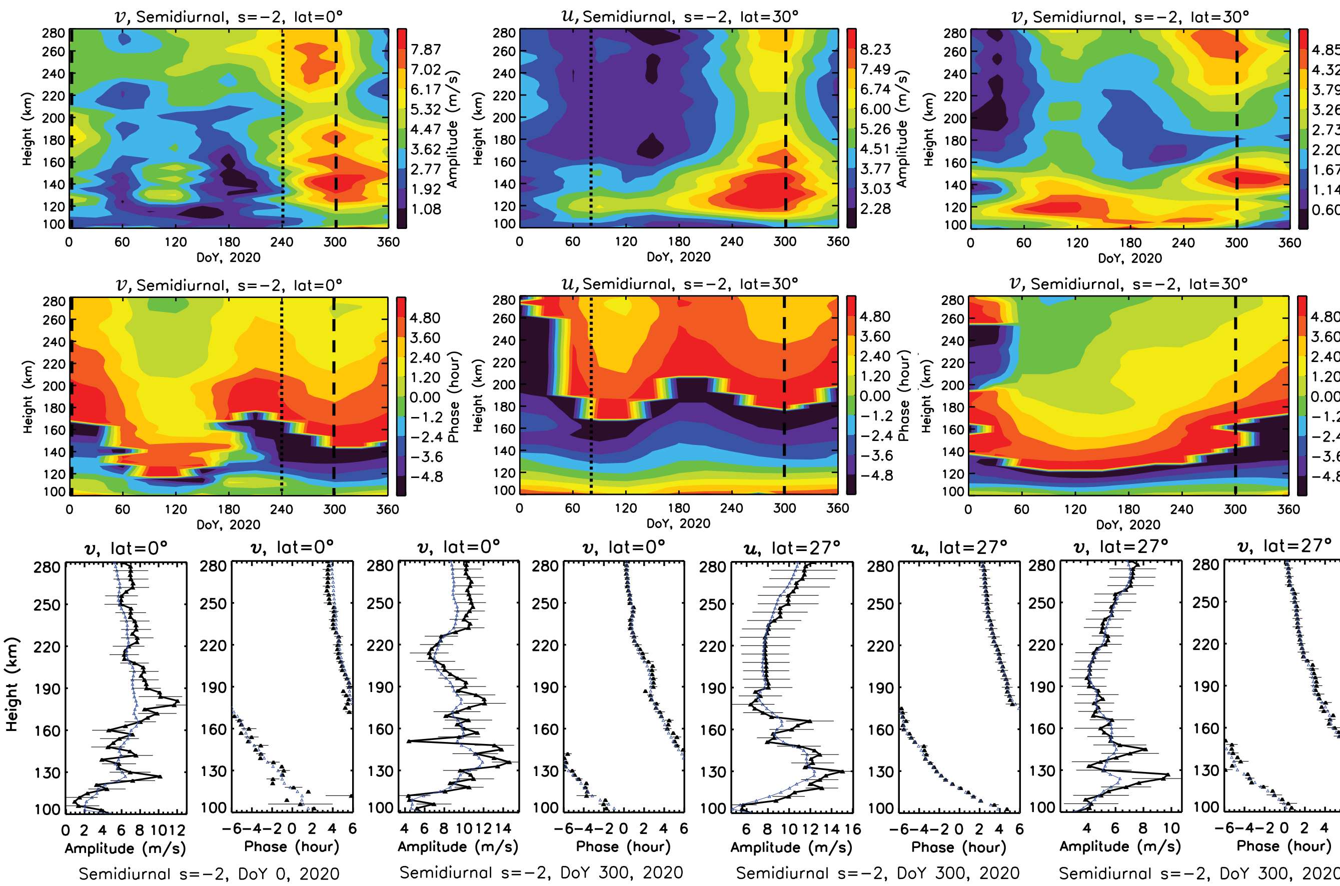

Figure 7. Top row: htvsdoy depictions of 61dm SE2 amplitudes at fixed latitudes. Left: v at 0 ° latitude. Middle: u at 30° latitude. Right: v at 30° latitude. Middle row: phases corresponding to amplitudes on the top row. Bottom row: amp/phz profiles corresponding to vertical dashed lines in top two rows in the following sequence: v at 0° latitude centered on DOY 0, v at 0° latitude centered on DOY 300, u at 27° latitude centered on DOY 300, v at 27° latitude centered on DOY 300. The vertical dotted lines in the top two rows correspond to vertical amp/phz profiles for v at 0° latitude centered on DOY 240 in Figure 5, and for u at 27° centered on DOY 80 in Figure 6. Refer to dashed lines in Figure 2 for latvsdoy context of these SE2 plots at 106 km and 250 km.

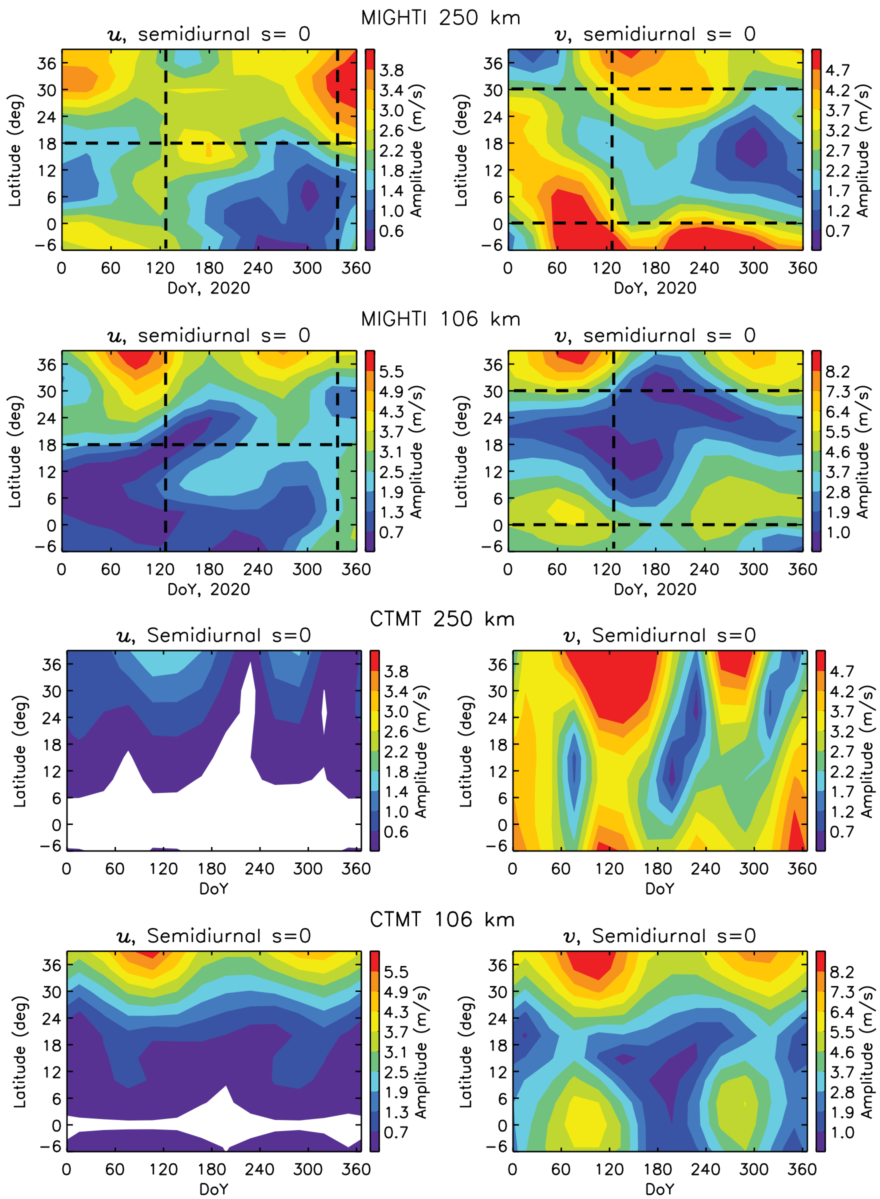

1280 **Figure 8.** Same as Figure 2, except for S0.

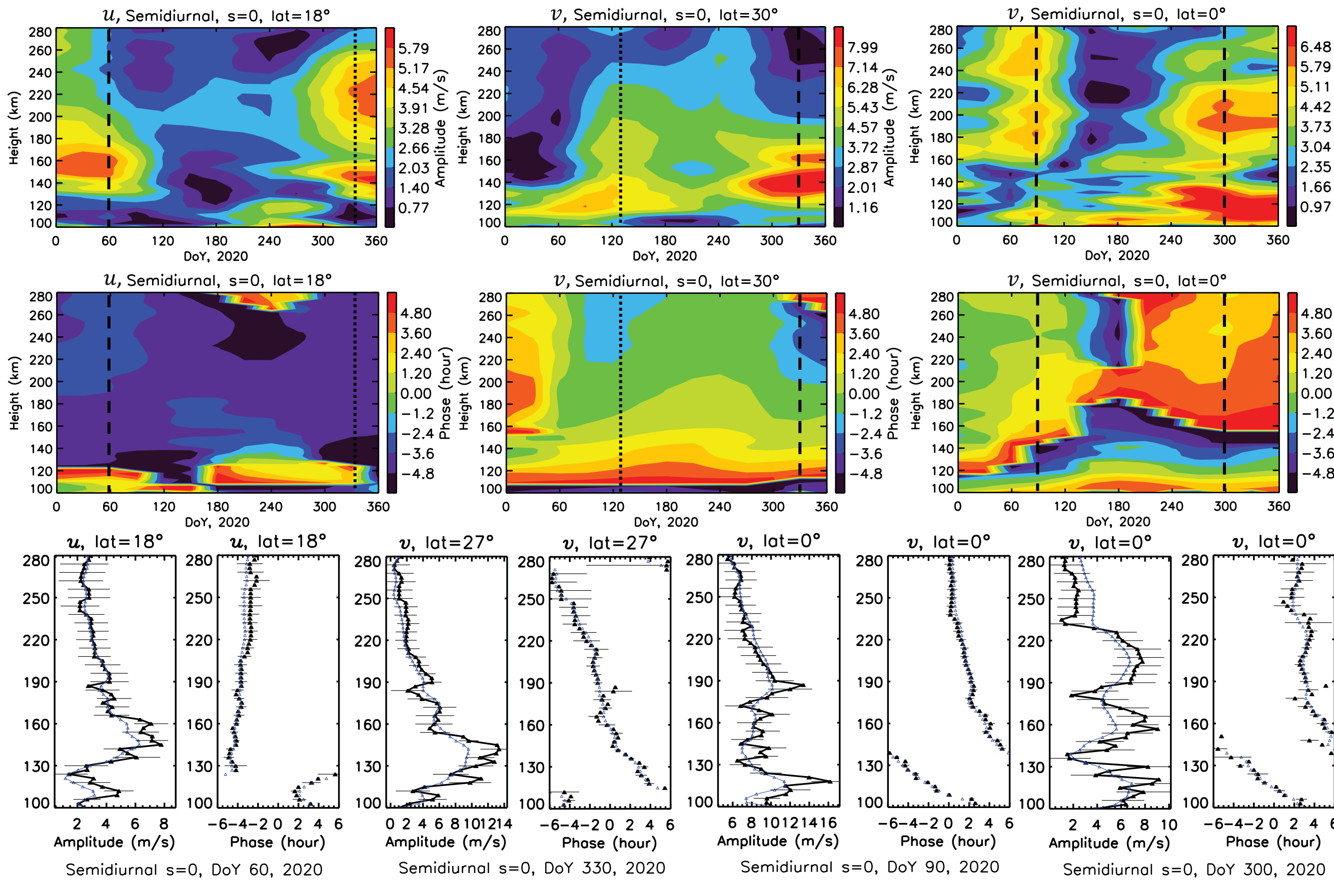

Figure 9. Same as Figure 7, with the following exceptions: Amplitude depictions in top row correspond to (left to right) S0 u at 18 $^\circ$ latitude, S0 v at 30° latitude, and S0 v at 0° latitude. The sequence of amp/phz profiles in the bottom row correspond to (left to right) S0 u at 18° latitude centered on DOY 60, S0 v at 27° latitude centered on DOY 330, S0 v at 0° latitude centered on DOY 90, S0 v at 0° latitude centered on DOY 300. The vertical dotted lines in the top two rows correspond to vertical amp/phz profiles for u at 18° latitude centered on DOY 340 in Figure 6, and for v at 27° latitude centered on DOY 125 in forthcoming Figure 10. Refer to dashed lines in Figure 8 for latvsdoy context of these S0 plots at 106 km and 250 km.

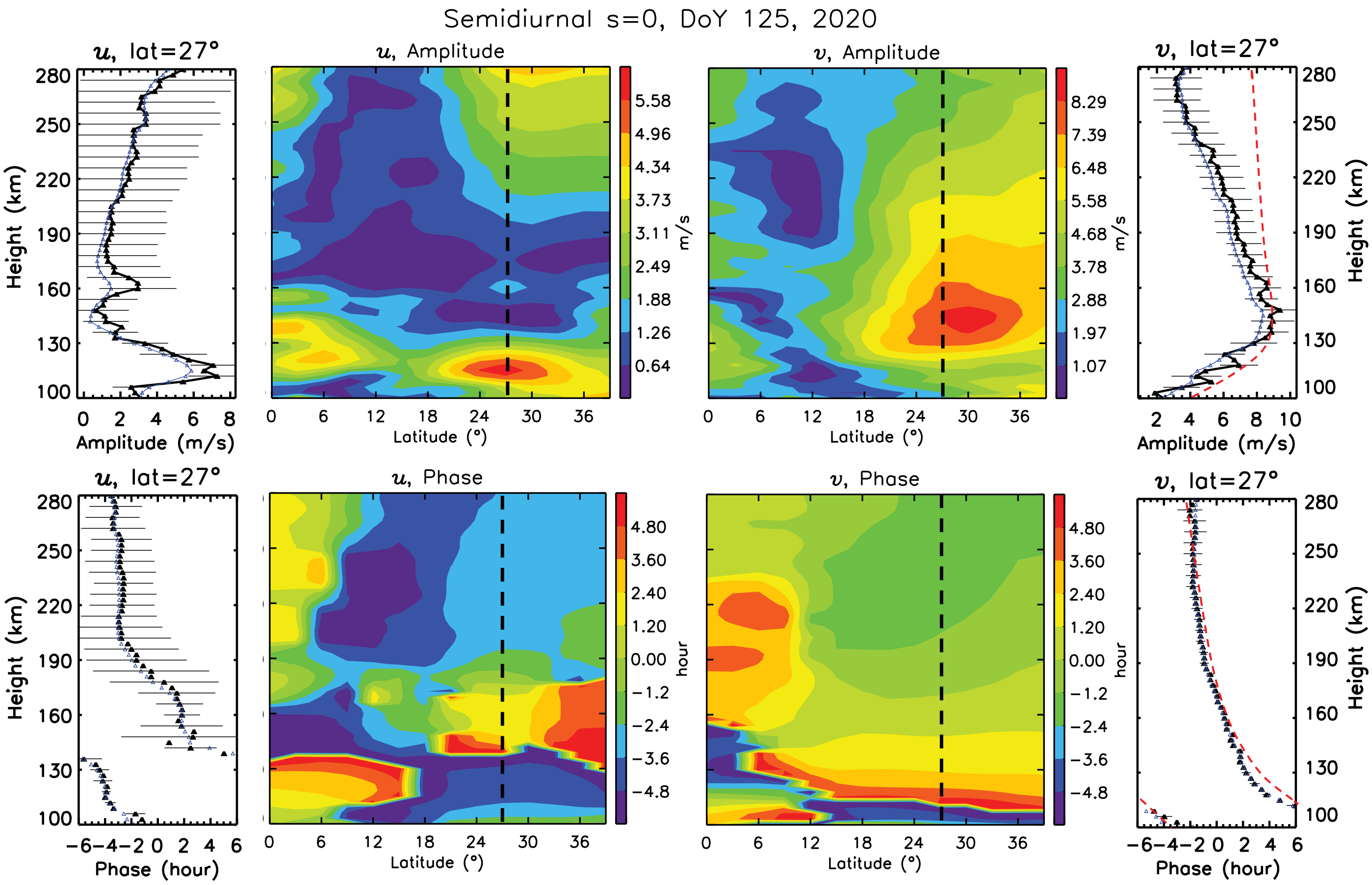

1289 **Figure 10.** Same as Figure 5, except for 41dm u and 41dm v for S0 centered on DOY 125,
1290 with vertical amp/phz profiles at 27° latitude. The red dashed lines in the v profiles on the right
1291 correspond to HME2, calibrated to agree with MIGHTI in the vicinity of the amplitude peak.

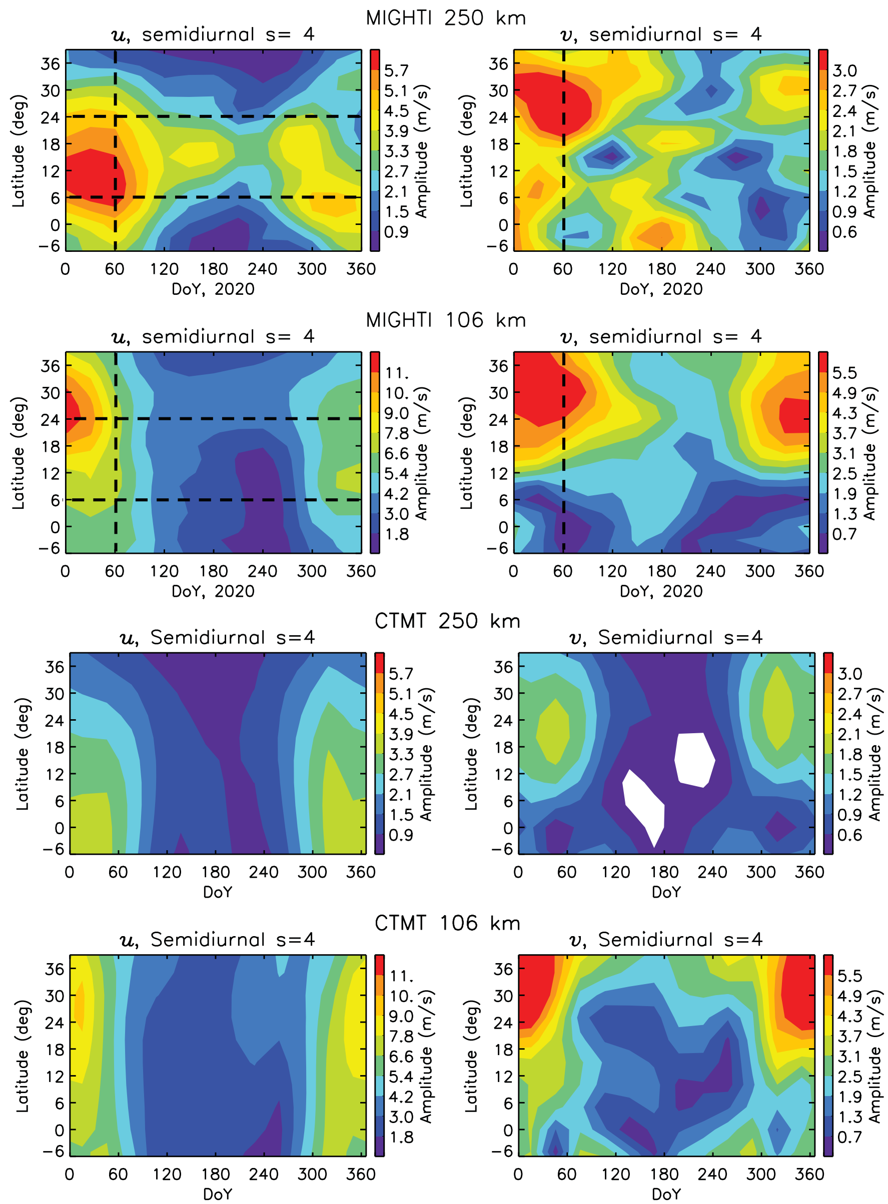

1292 **Figure 11.** Same as Figures 2 and 8, except for SW4.

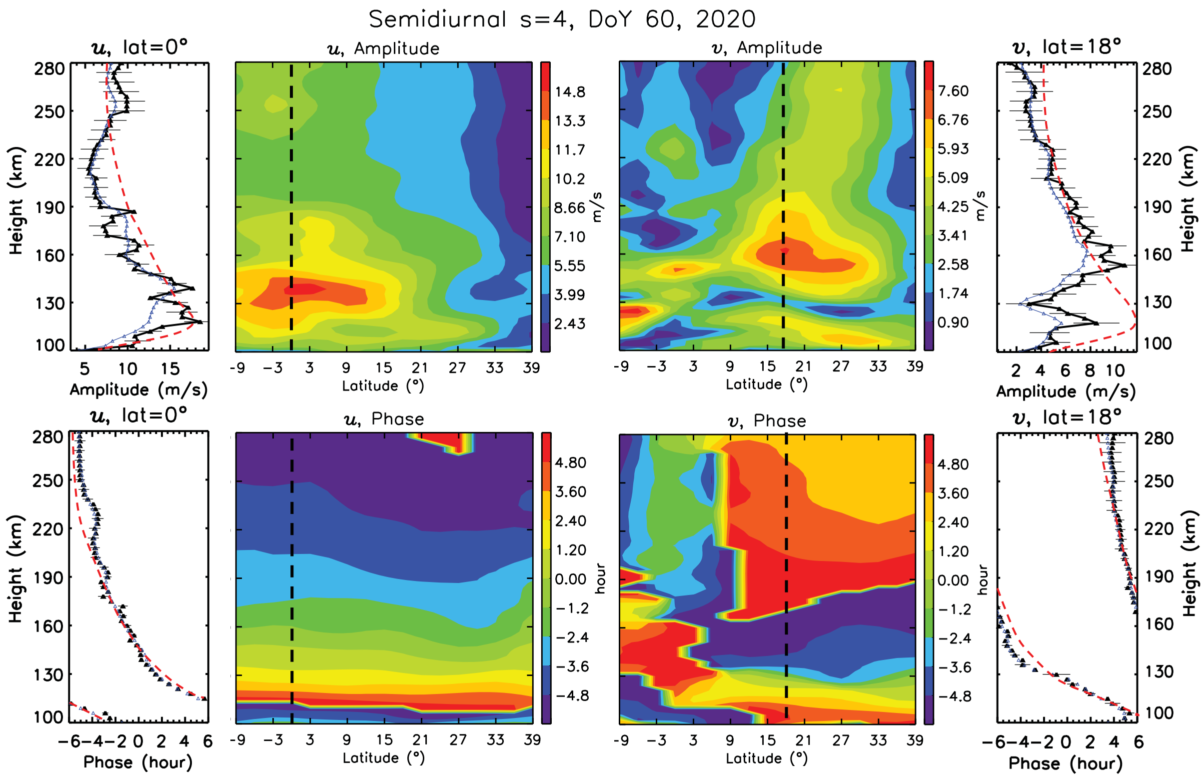

Figure 12. Same as Figures 5, 6 and 10, except for 41dm u and v for SW4 centered on DOY 60, with vertical amp/phz profiles for u at 0° latitude and for v at 18° latitude. The red dashed lines for u at 0° latitude in the profiles to the left represent HME1 calibrated to best fit the MIGHTI black profile in the vicinity of the amplitude peak. The red dashed lines in the v profiles at 18° latitude to the right are those *predicted* based on the HME1 amp/phz profiles for u at 0° latitude, assuming the internal consistencies in amplitude and phase between u and v at the two latitudes and at all heights within the theoretically-calculated HME1.

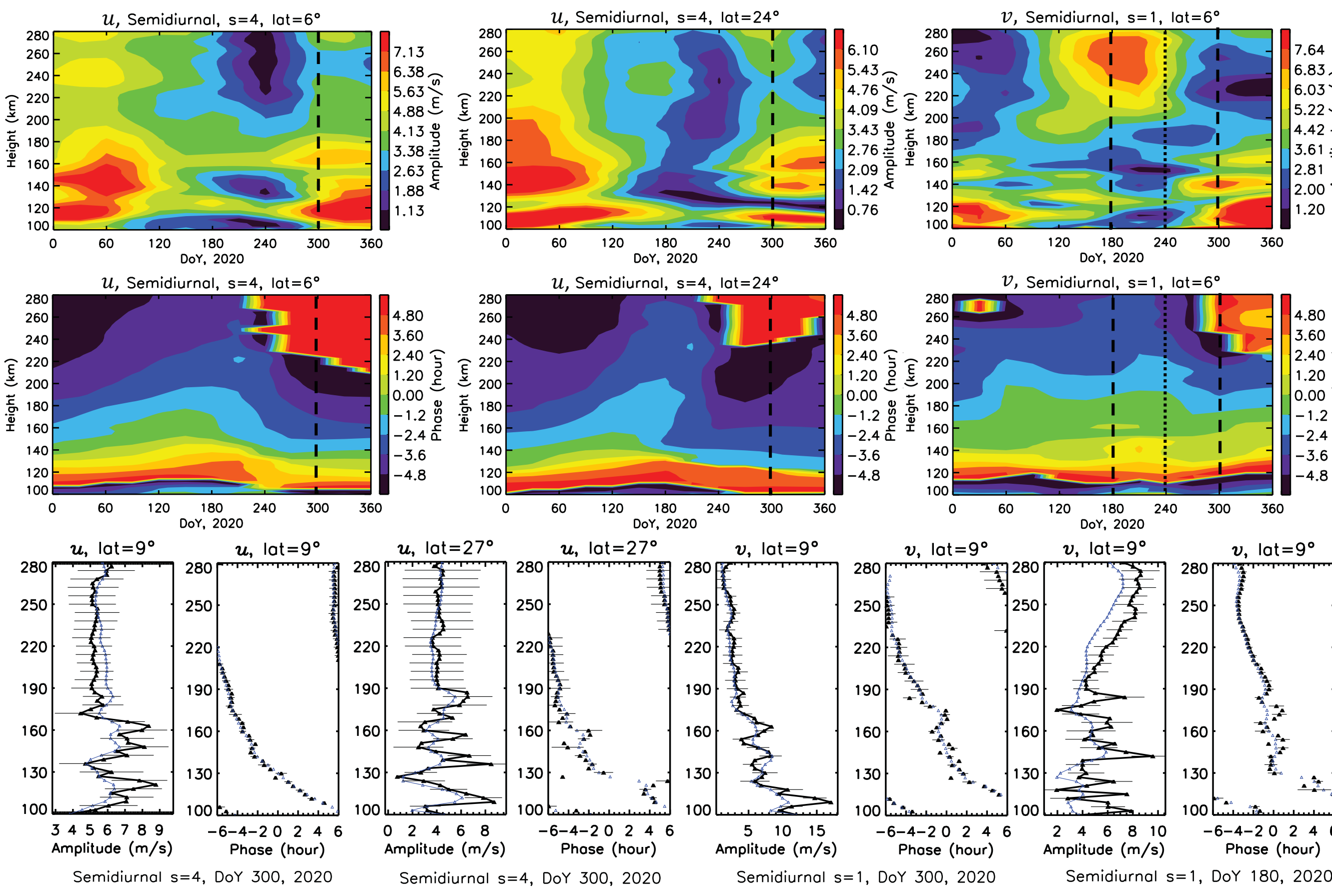

Figure 13. Same as Figure 7, with the following exceptions: Amplitude depictions in top row correspond to (left to right) SW4 u at 6° latitude, SW4 u at 24° latitude, and SW1 v at 6° latitude. The sequence of amp/phz profiles in the bottom row correspond to (left to right) SW4 u at 9° latitude centered on DOY 300, SW4 u at 27° latitude centered on DOY 30, SW1 v at 9° latitude centered on DOY 300, SW1 v at 9° latitude centered on DOY 180. The vertical dotted lines in the top two rows correspond to vertical amp/phz profiles for SW1 v at 9° latitude centered on DOY 240 in forthcoming Figure 15. Refer to horizontal dashed lines in Figure 11 for SW4 and forthcoming Figure 14 for latvsdoy context of these plots at 106 km and 250 km.

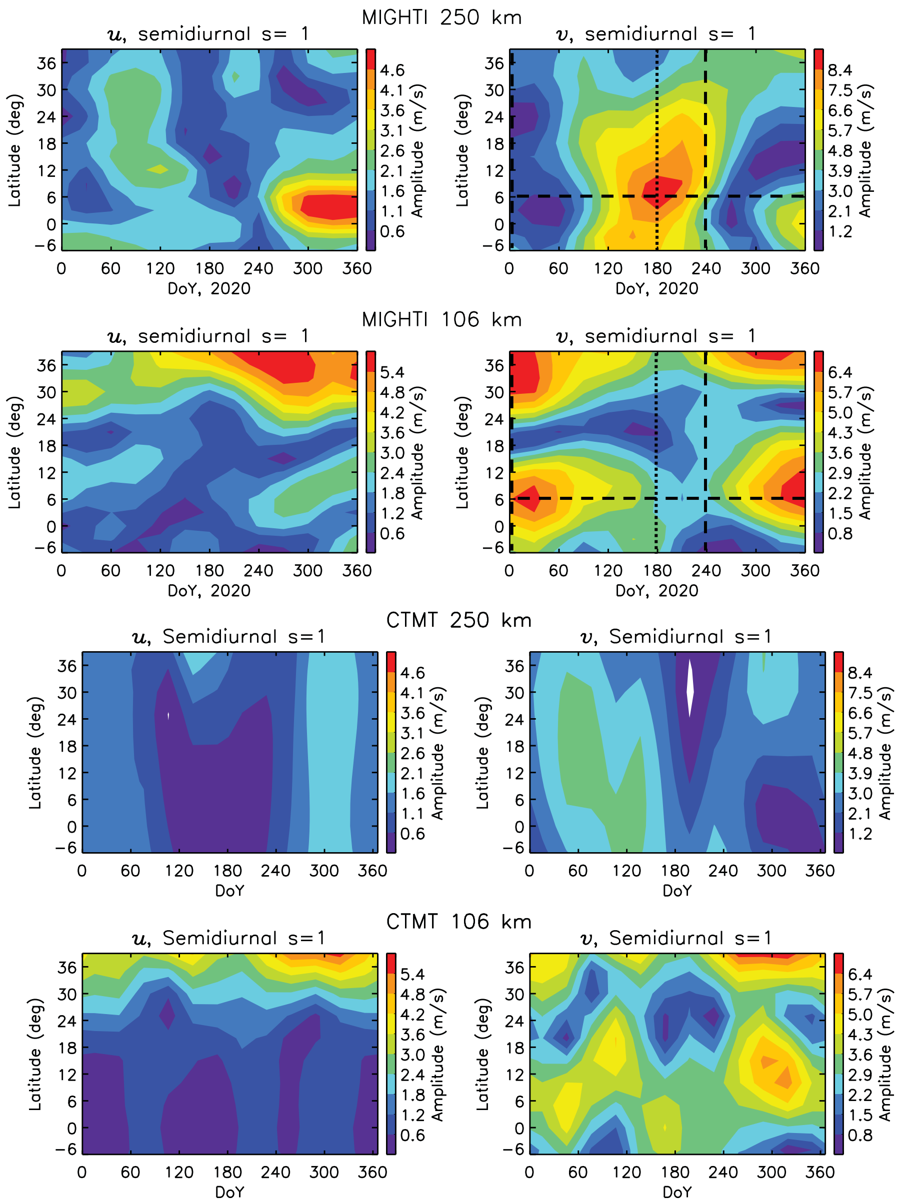

Figure 14. Same as Figures 2, 8, and 11, except for SW1. The vertical dashed lines at DOY 0 and DOY 240 refer to htvslat plots and profiles in Figure 15. The horizontal dashed line and vertical dotted line refer to htvsdoy and vertical profile plots in Figure 13.

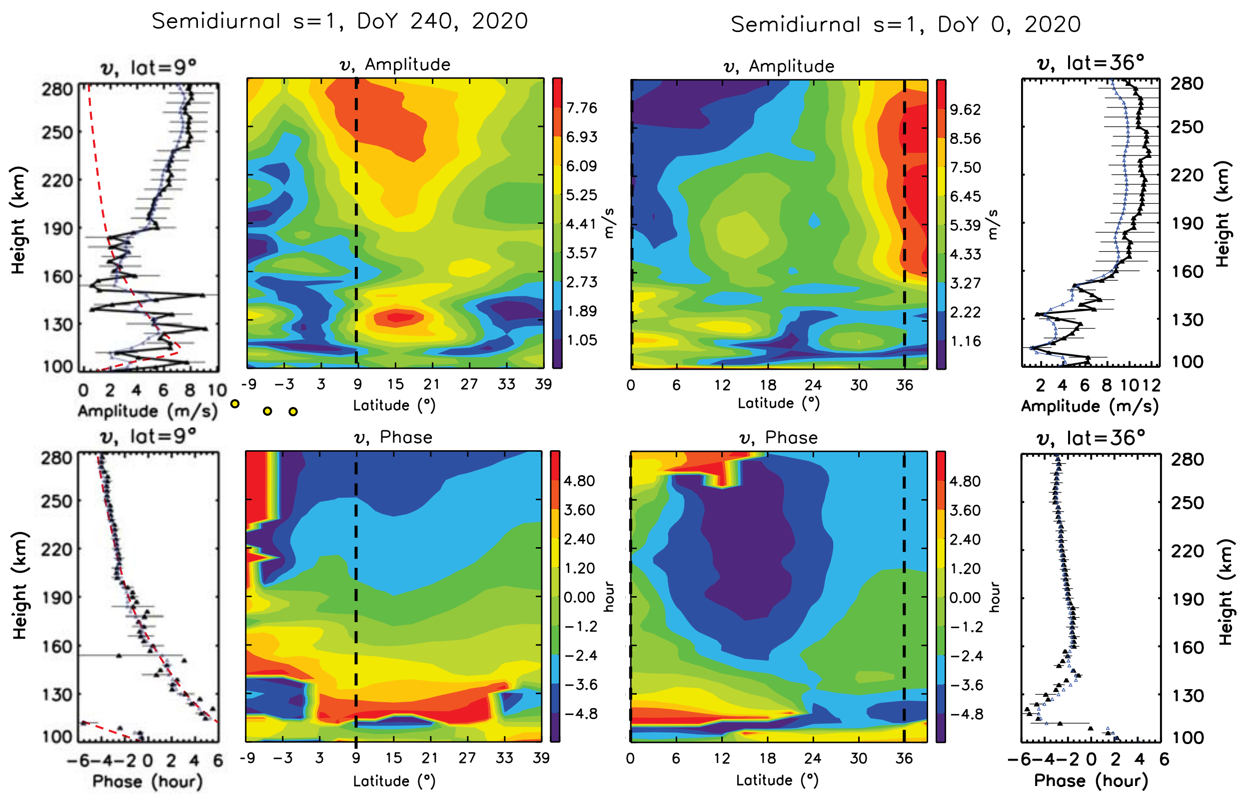

1311 **Figure 15.** Same as Figures 5, 6, 10, and 12, except for 61dm v for SW1 centered on DOY
1312 240 with vertical profiles at 9° latitude (left), and 41dm v for SW1 at DOY 0 with vertical pro-
1313 files at 36 ° latitude (right). The red dashed curves in the v profiles at 9° latitude to the left
1314 represent HME3 calibrated to best fit the MIGHTI amplitudes below 160 km.

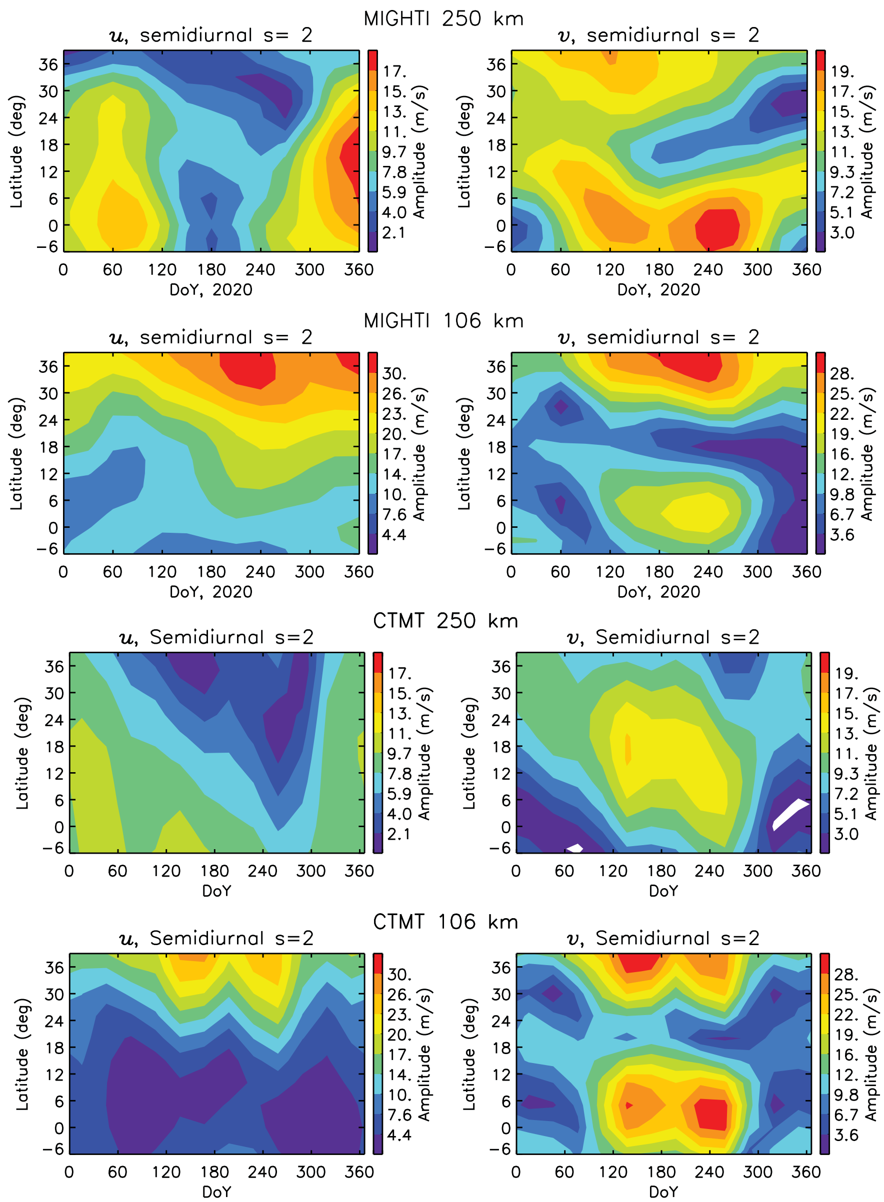

1315 **Figure 16.** Same as Figures 2, 8, 11, and 14, except for SW2.

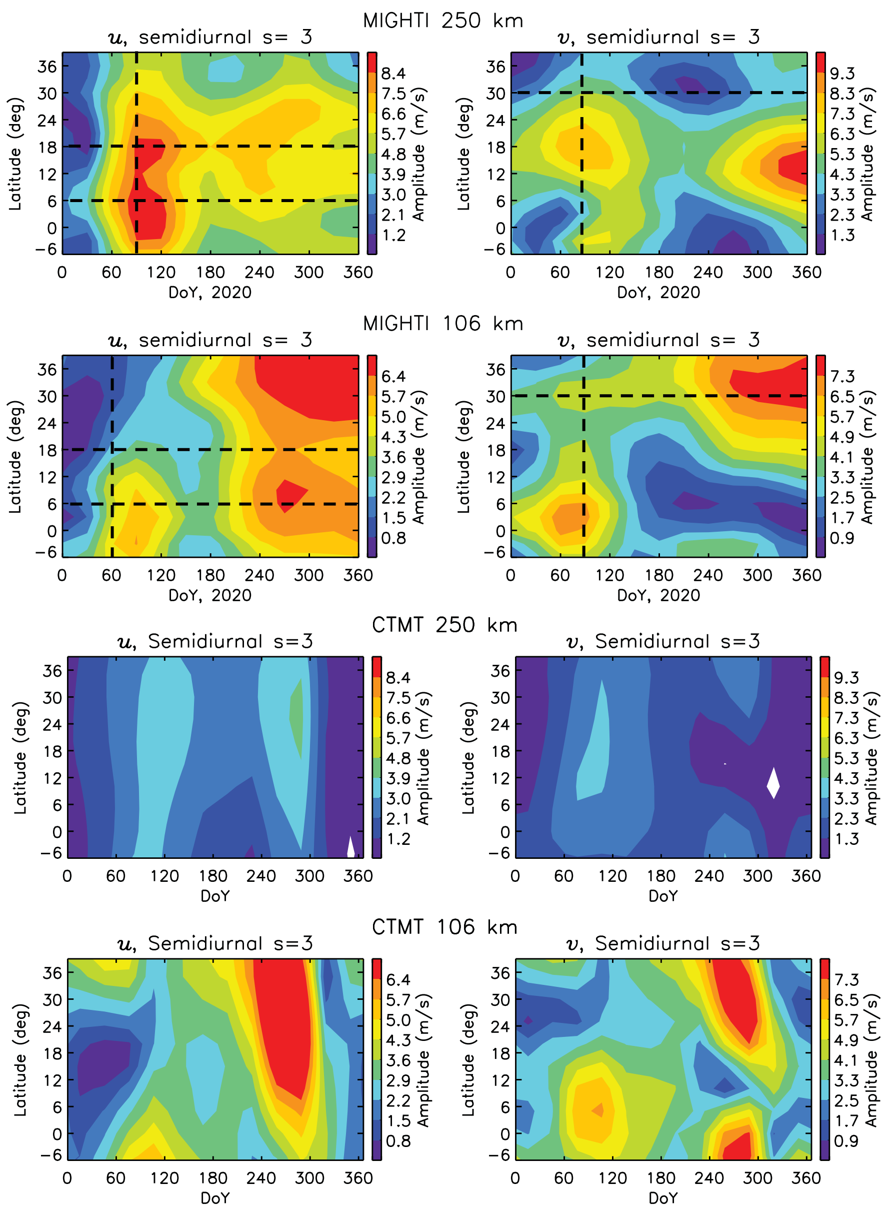

1316 **Figure 17.** Same as Figures 2, 8, 11, 14, and 16, except for SW3.

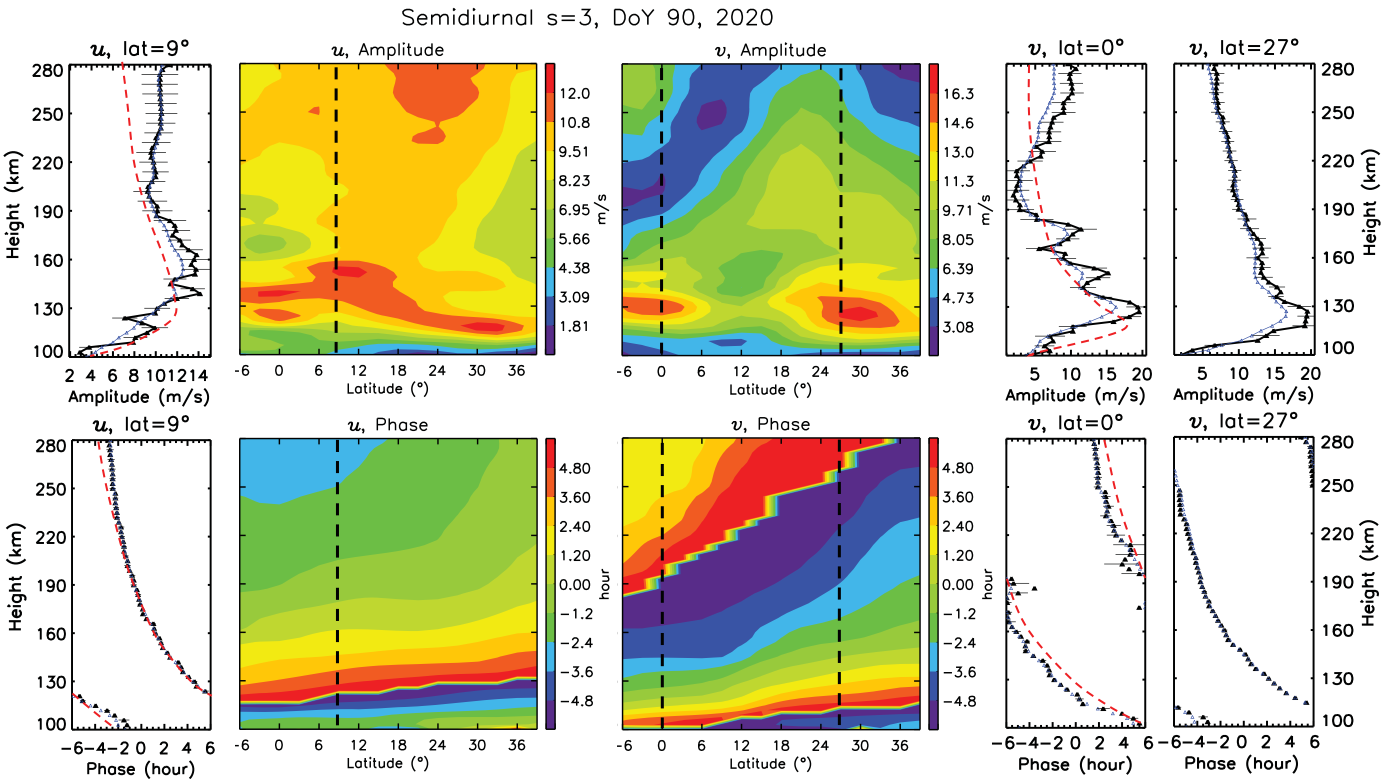

Figure 18. Same as Figures 5, 6, 10, 12, and 15 except for 61dm u for SW3 centered on DOY 90 with vertical profiles at 9° latitude (left), and 61dm v for SW3 at DOY 90 with vertical profiles at 0° and 27° latitude (right). The dashed red lines represent curves for HME1(HME2) in the profiles to the left(right), calibrated to best fit the MIGHTI profiles in the vicinity of the amplitude peaks.

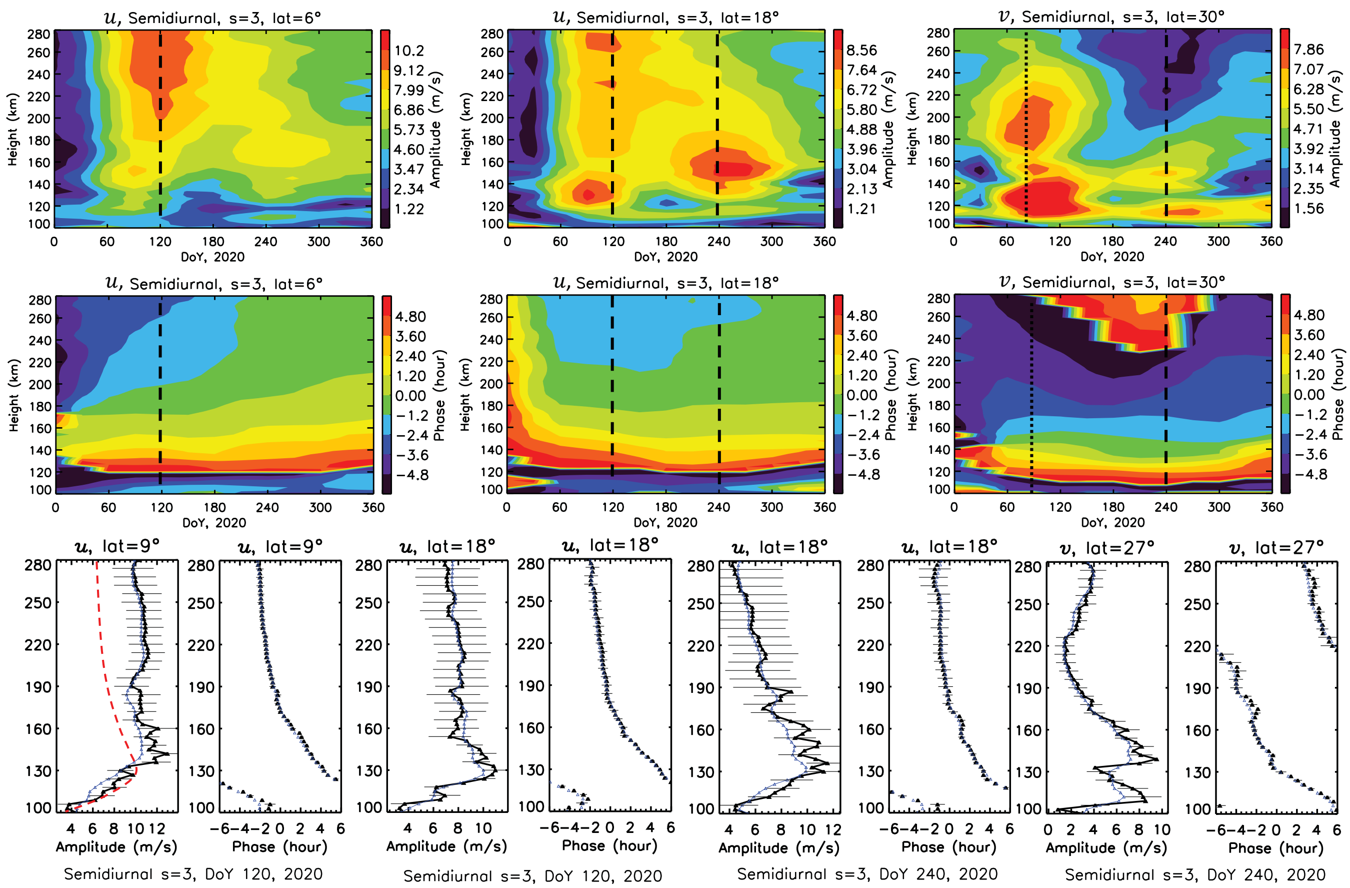

1322 **Figure 19.** Same as Figure 7, with the following exceptions: Amplitude depictions in top
1323 row correspond to (left to right) SW3 u at 6° latitude, SW3 u at 18° latitude, and SW3 v at 30°
1324 latitude. The sequence of amp/phz profiles in the bottom row correspond to (left to right) SW3
1325 u at 9° latitude centered on DOY 120, SW3 u at 18° latitude centered on DOY 18, SW3 u at 18°
1326 latitude centered on DOY 240, SW3 v at 27° latitude centered on DOY 240. The vertical dotted
1327 lines in the top two rows correspond to vertical amp/phz profiles for SW3 v at 27° latitude cen-
1328 tered on DOY 90 in Figure 18. Refer to horizontal dashed lines in Figure 17 for latvsdoy context
1329 of these plots at 106 km and 250 km.

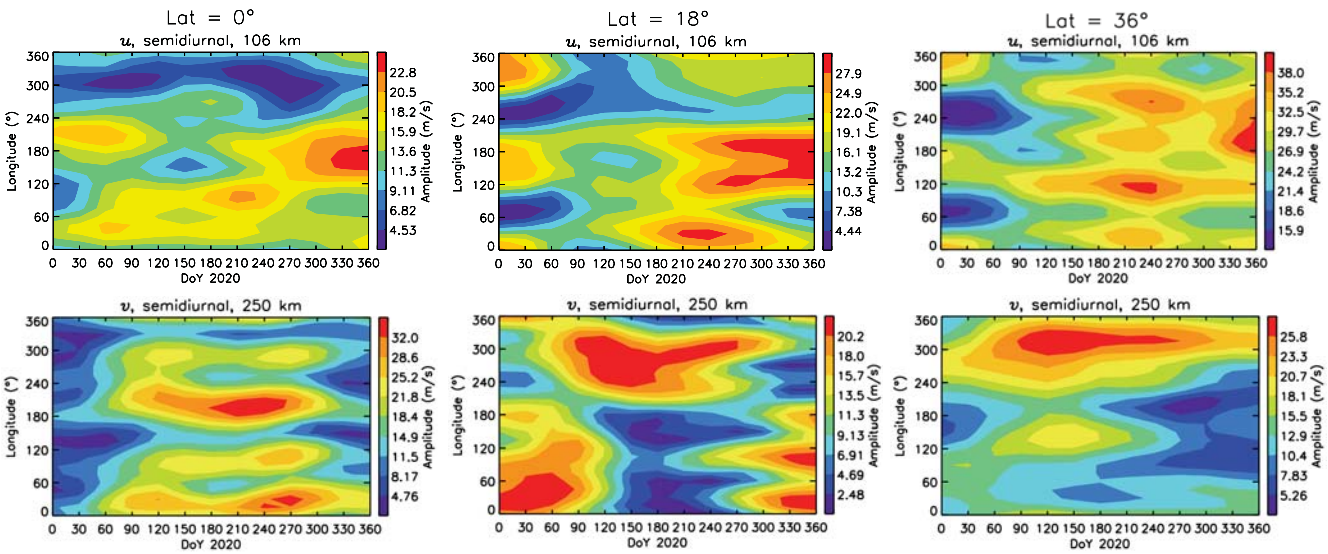

Figure 20. Lonvsdoy depictions of total (vector-mean) semidiurnal tidal amplitudes, obtained by superimposing SE2, S0, SW1, SW2, SW3 and SW4 for u at 106 km (top row) and v at 250 km (bottom row) at 0° latitude (left), 18° latitude (middle) and 36° latitude (right).